Development of a Low Noise Drone Propeller Using CFD Simulations

Axel Schulz

June 2023

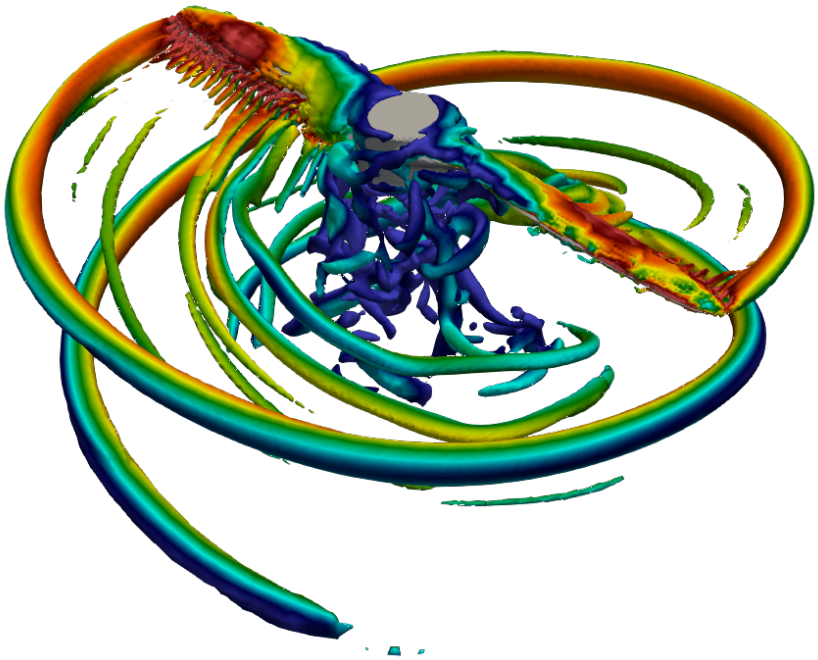

LUND
UNIVERSITY

This degree project for the degree of Master of Science in Engineering has been conducted at the Division of Fluid Mechanics, Department of Energy Sciences, Faculty of Engineering, Lund University.

Supervisor at the Division of Fluid Mechanics was Robert-Zoltán Szász.

Examiner at Lund University was Prof. Johan Revstedt.

Opponent at Lund University was Mitra Malekpour.

Department of Energy Sciences
Faculty of Engineering
Lund University

ISSN: <0282-1990>
LUTMDN/TMHP-23/5526-SE

Typeset in LaTeX
Lund 2023

Abstract

Noise pollution generated by drones has in recent years become a concern for humans and wildlife and has in some regions resulted in regulatory backlash. This thesis investigates the possibilities of developing a low noise drone propeller using computational fluid dynamics (CFD) simulations. A commercial drone propeller from the manufacturer APC Propeller has been modified with different forms of serrations to the trailing edge of the propeller. The simulations, conducted in the open source program OpenFOAM, using an LES turbulence model and an aeroacoustic analogy, shows promising results. The modified propellers shows an overall decreased sound pressure level compared to the unmodified propeller. However, the simulations do have some limitations and only covers a limited amount of working drone scenarios. Furthermore the modifications that are evaluated are only done to the trailing edge of the propeller. Overall the study shows promising results in using CFD to develop a low noise drone propeller. Future work could include modifications to the propeller in other locations than the trailing edge, and in a more varied set of working scenarios.

Acknowledgements

I would like to give my warmest thanks to my supervisor Robert-Zoltán Szász for his endless patience and support during this project. In times of uncertainty or when facing problems he has always provided me with encouragement and guidance, and this project would not have been possible without him. I am also very grateful for all that he has taught me about not only computational fluid dynamics, but also computers and software – knowledge which I think will serve me well in future work and in life.´

I would also like to thank the company APC Propellers for sharing their proprietary propeller data with me.

Contents

1 Introduction

1.1 Background

The last two decades saw a rapid increase in the usage of small unmanned aerial vehicles (SUAV), or more commonly called drones. From initially being used mainly in military settings, drones can today be found in various commercial applications such as surveillance, transportation, and photography. With the number of drones in the urban sky still being quite few, the reader might not know that drones are noisy. The noise from a drone is often a high-frequency broadband noise that researchers suggest is more annoying to humans than the noise from road traffic or airplane traffic noise [1]. Both the noise and the annoyance can be hindrance to smooth operations in various fields of application. The noise emitted from drones has already resulted in drones being banned from urban environments and national parks at some places around the world, to protect humans and wildlife. [2]

With the numerous potential usage areas for drones, more and more people turn to drones to solve their specific problems. The North American commercial drone market as of 2021, had an estimated market size value of $ 20.8 billion. It is forecasted that the same market in 2028 will have an estimated value of $ 501.4 billion. [3] The large growth of the industry can only be possible if drones are not hit with widespread regulatory backlashes such as noise regulations.

The noise generated by drones comes mainly from the small propeller blades and their interaction with the turbulent wakes generated by the rotational movement, which often has a velocity of several thousand revolutions per minute. To reduce the noise generated, the interaction between the propeller blade and the wake must be altered in some way. Thankfully, nature has had this problem before us, and has proposed some solutions. The common Barn Owl (*Tyto Alba)* and Barred Owls (*Strix Varia*), are birds that have been studied for their near silent flight. [4] This allows them to stalk and hunt pray easily during the night. What makes their flight so silent, is certain characteristics of their wings, which greatly inhibits the noise emitted during flight. Researchers have identified that one of the characteristics responsible for making the owl's wings so silent during flight, is the presence of serrations on the trailing edge of each wing. Looking to nature for inspiration when it comes to engineering solutions is nothing new – there is a whole field dedicated to this called Biomimetics.

1.2 Purpose & Objective

The purpose of this thesis is to develop and evaluate a low noise drone propeller using computerised tools and analysis methods such as CAD (Computer Aided Design) and CFD (Computational Fluid Dynamics). The starting point will be a commercially available drone propeller from the company APC Propellers. The propeller will then be modified with features initially similar to those found on the wings of owls. The original and the modified propellers are then to be evaluated in the open source CFD software OpenFOAM, to see the noise characteristics of both propellers.

1.3 Project Delimitations

This project is limited by certain factors such as time and computational power. Because of this the drone propeller will only be modified at the trailing edge. The modifications will not be evaluated with any parameter study, and the propeller performance will not be studied during different flight scenarios except for one – a base scenario of stationary flight at a propeller rpm of 3600. All testing will be confined to the computer realm.

2 Theory

2.1 Propellers

The use of propellers to generate lift and forward thrust can be traced back to the end of the 15th century, when Leonardo Da Vinci proposed a helicopter design driven by a large airscrew. This design was never realised. In the centuries following, various designs for powered flight machines were proposed and tested, but the majority were unsuccessful. The first successful, controlled and sustained flight in a vehicle heavier than air, is contributed to the Wright brothers. The Wright brothers were brilliant self trained engineers and used a propeller made out of spruce wood lamination. This early propeller had a remarkably accurate propeller calculation, with the propeller twist being correct for the speed ratio for their propeller. [5] In essence, the basic characteristics of the propeller the Wright brothers used, is the same as in modern propellers.

2.2 Propeller Basics

An aeronautic propeller produces thrust or lift (depending on usage) by rotational movement through the air. Basically the propeller can be seen as a rotating wing. A cross sectional view of a propeller will reveal an airfoil shape. The *modus operandi* by which the airfoil actually produces lift has been a subject of great debate. Proponents of different theories usually cite either Newtonian physics and explains lift as a reaction force from the deflection of the air on the airfoil, or the principles of Bernoulli which explain lift as the result of pressure differences across the airfoil. The truth is that lift force generated by an airfoil is complex phenomena that is hard to simplify and that both points of view can be seen as correct. [6] It can be stated that lift force is generated by turning a moving fluid. Newton's second law states:

$$\vec{F} = m\vec{a} \tag{1}$$

If the acceleration is rewritten using the material acceleration, as:

$$\vec{F} = m\frac{d\vec{v}}{dt} = m(\frac{\partial\vec{v}}{\partial t} + u\frac{\partial\vec{v}}{\partial x} + v\frac{\partial\vec{v}}{\partial y} + w\frac{\partial\vec{v}}{\partial z}) \tag{2}$$

it is apparent that changing the speed or direction of a fluid flow will result in a force. [7] The lift force generated by an airfoil is dependent on the geometry and profile of the airfoil. Altering an airfoil will invariably change the performance characteristics of it. It might therefore be a challenge to modify the design of a wing or propeller to optimize for a certain metric without seeing a drop in performance of another metric, such as lift force.

A difference between a propeller and a wing, is that a propeller has a varied cross-sectional airfoil chord angle. This is called propeller twist. The twist results in different angles of attack, which is the angle between the airfoil chord and the direction of the airflow. By looking at the formula for angular velocity:

$$v = r \cdot \omega \tag{3}$$

it is evident that the airflow velocity is not constant throughout the propeller. By changing the airfoil chord angle throughout the radius of the propeller, the angle of attack is optimized throughout the radius. This is the reason for the propeller twist.

2.3 Sound & Noise Emission

Physically, sound and noise is the result of small pressure fluctuations in the air (or any other propagating medium) as processed by the human ear. These pressure fluctuations are often generated by a vibrating surface or object, but can also be the result of turbulent mixing – or vortexes – in the air. The pitch perceived by the ear is dependent on the frequency of the pressure fluctuations. Just as a large object with slow vibrations induce a lower pitched sound, larger vortexes also generate a lower pitched sound and vice versa. A turbulent energy cascade with its vortexes in decreasing sizes, results in a broadband noise.

When modelling sound it is important to consider that not all sound sources are equal. A single point emitting sound in all directions is referred to as a monopole. Two opposite monopoles of equal strength placed together, creates a source that generates sound in an opposite phase. This is referred to as a dipole, and an example of this would be a speaker membrane. If two opposite dipoles of equal strength are combined, the result is a quadrupole. Quadrupoles are generated by turbulent vortices in flows. It is from quadrupoles that energy is converted into sound aerodynamically, for example from the mixing region of a jet exhaust or behind the trailing edge of a high speed propeller. [8]

The noise emitted from a drone is dominated by the noise emitted by the propellers. Propeller noise is a function of the geometry of the propeller, blade loading and the number of blades. The main contributor however, is the propeller tip speed. [9] In the case of commercial drones, the small propellers that are commonly used create a broad spectral noise in the low to mid frequency spectrum. The noise is dominated by the tones resulting from the blade pass frequency, and the resulting harmonics. [1] There is also a broad band component [10], as seen in the Fourier domain. In order to develop strategies to minimise the propeller noise, it is necessary to study what causes the noise. As previously mentioned, the propeller noise is composed of tonal self-noise from the blade pass frequency and a broad band component. The self-noise is generated by the volume displacement caused by the blade, and the aerodynamic loading on it. [11] The broad band noise is generated not so much from the propeller tip, but more from the leading and trailing edge of the blade. The trailing edge produces turbulence and vortex shedding. The leading edge interacts with this turbulent flow and a feedback mechanism is created. This can be seen in Figure 1 The noise causing turbulence is therefore created both at the leading and the trailing edge. [11] With the noise creating mechanisms in mind, it seems reasonable to modify either the tip, trailing or leading edge or entire profile of a blade in order to improve the desired sound characteristics.

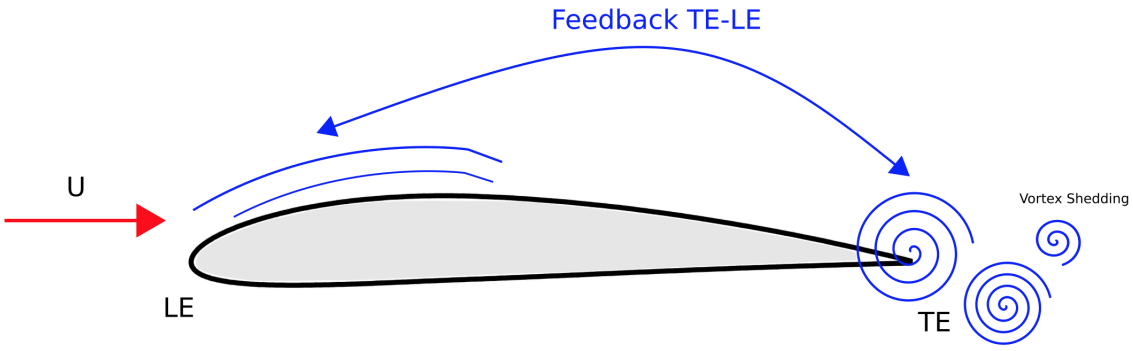

Figure 1: Airfoil Cross Section Showing the Feedback Mechanism Between Leading and Trailing Edge

2.4 Computational Fluid Dynamics

Computational Fluid Dynamics, or *CFD*, is a powerful technique for calculating fluid flow, heat transfer and similar phenomena. The CFD calculations are made using numerical algorithms to solve the fluid flow problems. The problems that can be solved using CFD spans a wide range and include among others: aerodynamic analysis of cars and aeroplanes, chemical process engineering and weather prediction in meteorology. With the increasing use of computers and the exponential increase of computing power during the 20th century, CFD has come to replace many previous physical models, such as wind tunnels, in the design and R&D processes in many industries. [12]

To attain numerical solutions to the fluid flow problems in CFD, the fluid flows are modelled using mathematical equations. The equations are then solved using numerical techniques, resulting in approximate solutions to the problems. The solutions can reveal the characteristics of the fluid flow. The equations governing the physics of a CFD problem are commonly refered to as the *Governing Equations*.

2.5 Governing Equations

The governing mathematical equations used in computational fluid dynamics stem from the premise that the physical properties of a fluid are conserved. This is summarised in the conservation laws of physics, which are:

- The total mass of a fluid in a system is conserved.
- The rate of change of a fluid particle's momentum, is equal to the sum of the forces acting on the particle.
- The energy change for a fluid particle, is equal to the change rate of thermal energy and the rate of work for the particle.

These three conservation laws are appropriately divided and named (in order) the *Mass Conservation*, the *Momentum Conservation* and the *Energy Conservation*.

The **Mass Equation** is based on the fact that for a fluid element, the rate of the increase of mass in the element, must be equal to the net rate of flow of mass into the element. In the 3D case with a compressible fluid, that is:

$$\frac{\partial}{\partial t}(\rho \delta x \delta y \delta z) = \frac{\partial \rho}{\partial t} \delta x \delta y \delta z \tag{4}$$

This equation can be rewritten in multiple steps to further highlight the net rate of mass flow into the element across its faces. The full derivation is beyond the scope of this theory section. The final rewritten equation can be seen in equation 5 below.

$$\frac{\partial \rho}{\partial t} + \frac{\partial(\rho u)}{\partial x} + \frac{\partial(\rho v)}{\partial y} + \frac{\partial(\rho w)}{\partial z} = 0 \tag{5}$$

Equation 5 can be and is commonly rewritten on the more compact vector notation form:

$$\frac{\partial \rho}{\partial t} + \text{div}(\rho \mathbf{u}) = 0 \tag{6}$$

The next equation used in CFD is the **momentum equation**. Earlier it was stated that the rate of change of a fluid particle momentum is equal to the sum of the forces acting on the particle. This is indeed true and the rate of change for a fluid particle per unit volume is expressed as:

$$\rho \frac{Du}{Dt}, \quad \rho \frac{Dv}{Dt}, \quad \rho \frac{Dw}{Dt} \tag{7}$$

This is for x-, y-, and z-momentum respectively. When it comes to the forces acting on the fluid particles, there are different types of forces. These forces are often divided in to two categories: surface forces and body forces. The surface forces are forces such as pressure force, viscous force and gravity force. The body forces are forces like centrifugal force, Coriolis force and electromagnetic force. As in classical solid mechanics, pressure is denoted with p. Whereas solid mechanics often is concerned with shear stress on surfaces, CFD and its *fluid* elements has viscous stresses which are denoted with τ.

Expressed as an equation, where the rate of change of the fluid particles momentum equals the sum of the forces acting on the element, the momentum equation in its three components for the **x**-, **y**- and **z**-direction becomes:

$$\rho \frac{Du}{Dt} = \frac{\partial(-p + \tau_{xx})}{\partial x} + \frac{\partial \tau_{yx}}{\partial y} + \frac{\partial \tau_{zx}}{\partial z} + S_{Mx} \tag{8}$$

$$\rho \frac{Dv}{Dt} = \frac{\partial \tau_{xy}}{\partial x} + \frac{\partial(-p + \tau_{yy})}{\partial y} + \frac{\partial \tau_{zy}}{\partial z} + S_{My} \tag{9}$$

$$\rho \frac{Dw}{Dt} = \frac{\partial \tau_{xz}}{\partial x} + \frac{\partial \tau_{yz}}{\partial y} + \frac{\partial(-p + \tau_{zz})}{\partial z} + S_{Mz} \tag{10}$$

in which τ are the stress components in different directions, S_M are source terms and D represent the material derivative for a fluid particle. The last of the three governing equations used in CFD is the **energy equation**. In the same way as in the momentum equation, it is appropriate to study the energy of a single fluid particle and derive the equations from there. The energy equation stems from the first law of thermodynamics and states that the rate of increase of energy for a

fluid particle is equal to the net rate of heat added to the fluid particle as well as the net rate of work contributed to the fluid particle. The rate of increase of energy for a particle is given by the term:

$$\rho \frac{DE}{Dt} \tag{11}$$

with terms for the internal (thermal) energy, the kinetic energy and the gravitational potential energy, the resulting energy equation is:

$$\begin{aligned} \rho \frac{DE}{Dt} = -\text{div}(p\mathbf{u}) + \Bigg[& \frac{\partial(u\tau_{xx})}{\partial x} + \frac{\partial(u\tau_{yx})}{\partial y} + \frac{\partial(u\tau_{zx})}{\partial z} + \frac{\partial(v\tau_{xy})}{\partial x} \\ & + \frac{\partial(v\tau_{yy})}{\partial y} + \frac{\partial(v\tau_{zy})}{\partial z} + \frac{\partial(w\tau_{xz})}{\partial x} + \frac{\partial(w\tau_{yz})}{\partial y} + \frac{\partial(w\tau_{zz})}{\partial z} \\ & + \text{ div}(k \text{ grad } T) + S_E \end{aligned} \tag{12}$$

In equation 12, on the right hand side, the first and second term is the the total rate of work done per unit volume by all surface stresses. The third term is the rate of heat addition, from heat conduction, into the fluid element.
The shear stresses in the momentum governing equations can be rewritten. The result of this substitution is called the **Navier-Stokes Equations**. These equations are:

$$\rho \frac{Du}{Dt} = -\frac{\partial p}{\partial x} + \text{div}(\mu \text{ grad } u) + S_{Mx} \tag{13}$$

$$\rho \frac{Dv}{Dt} = -\frac{\partial p}{\partial y} + \text{div}(\mu \text{ grad } v) + S_{My} \tag{14}$$

$$\rho \frac{Dw}{Dt} = -\frac{\partial p}{\partial z} + \text{div}(\mu \text{ grad } w) + S_{Mz} \tag{15}$$

and are common and useful equations for the next step in the CFD process, which is the discretisation process. By introducing the continuity equation:

$$\frac{\partial \rho}{\partial t} + \text{div}(\rho \mathbf{u}) = 0 \tag{16}$$

the generic transport equation can be established:

$$\frac{\partial(\rho\phi)}{\partial t} + \text{div}(\rho\phi\mathbf{u}) = \text{div}(\Gamma \text{ grad } \phi) + S_\phi \tag{17}$$

In equation 17, ϕ is a general variable, and Γ is a diffusion coefficient. Sometimes "grad" and "div" is replaced with the math symbol nabla, ∇.

2.6 Finite Volume Discretisation

The Navier-Stokes equations lack analytical solutions except in rare cases. Because of this it is necessary to solve them numerically instead, and this is done by splitting the geometry into discrete, finite volumes. Using the generic transport equation presented in the previous section, the finite volume discretisation process begins with an integration over a three dimensional control volume:

$$\int_V \frac{\partial(\rho\phi)}{\partial t} dV + \int_V \text{div}(\rho\phi\mathbf{u}) dV = \int_V \text{div}(\Gamma \text{ grad } \phi) dV + \int_V S_\phi dV \tag{18}$$

These volume integrals are then rewritten using the Gauss's divergence theorem. When dealing with transient problems it is also necessary to take the time aspect into account and this is done by integrating once again over a sufficiently small time step, Δt. The final, and most general form of the transport equation is:

$$\int_{\Delta t} \frac{\partial}{\partial t} (\int_{CV} \rho\phi dV) dV + \int_{\Delta t} \int_A \mathbf{n}.(\rho\phi\mathbf{u}) \mathrm{d}A\mathrm{d}t = \int_{\Delta t} \int_A \mathbf{n}.(\Gamma \mathrm{grad}\phi) \mathrm{d}A\mathrm{d}t + \int_{\Delta t} \int_{CV} S_\phi \mathrm{d}V\mathrm{d}t \tag{19}$$

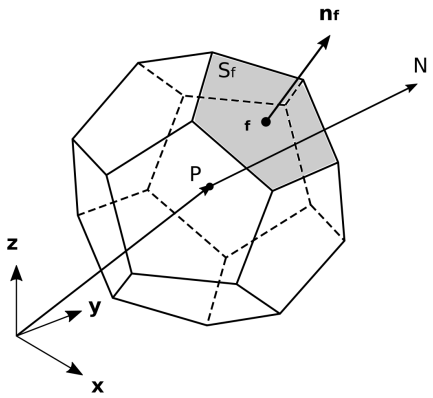

Figure 2: Volume Element

A figure of a generic volume element can be seen in Figure 2. Solving the Navier-Stokes equations numerically means solving the partial differential equations at certain points over the geometry or model that is computed. These fields – ϕ in above equations – are fields that are selected on the discretised finite volumes. By discretisation, the values of ϕ in and on different volume elements are converted from partial differential equations into algebraic equations, which are then solved numerically. Neighbouring cells are connected to each other via their shared element faces. There are different types of meshes used for volume elements and some are: [13]

- Cartesian
- Non-Orthogonal
- Block Structured Grids
- Unsctructured Grid
- Chimera Grids

2.7 Solution Algorithms

From the discretised geometry and its finite volume elements, a set of algebraic linear equations are generated. These equations are on the familiar matrix form:

$$\mathbf{A} = \phi\mathbf{B} \tag{20}$$

where matrix A contains the information from the generated mesh and the lineratsation. B contains the source terms, boundary conditions and constants. ϕ is the unknown cell value located in the centre of each volume element.

The variation between adjacent cells value of ϕ is assumed linear. This linearity can modelled in different ways. Some common ways, or discretization schemes, are the *upwind* and *central difference* scheme.

The system of equations generated in the discretisation process can be solved either through a direct or an iterative process. When dealing with transient flows, and CFD in general, the coefficients generated in the equations depend on the previous solution. Therefore the iterative process is the most widely used for CFD applications. Another reason is that the iterative process is computationally much lighter – the direct process requires more memory. There are multiple algorithms available to solve the equations and the ones that are most suited depends on the different case, and factors such as whether the fluid is compressible or not, and if the problem is of a transient or stationary character. [14]

One of the most common iterative algorithms for solving flow problems is the SIMPLE algorithm. **SIMPLE** (Semi-Implicit Method for Pressure Linked Equations) is a pressure method in which the pressure is calculated through a guess-and-correct procedure where the initial pressure is guessed. Then the momentum equation in equation 16 is solved, and after that the pressure correction equation, which is derived from the continuity equation. Pressure and velocity is then corrected and lastly the mass conservation is checked. This procedure is then repeated until convergence is achieved.

Another algorithm that is commonly used is **PISO** (Pressure Implicit with splitting of Operator). PISO was initially developed to be used with transient incompressible flows. This algorithm can be seen as an extension of the SIMPLE algorithm. It involves one predictor step and two correction steps, and the main difference is that is only solves the first step of the SIMPLE algorithm, the predictor step once. Like SIMPLE, it then solves the corrector steps iteratively until it both the momentum and the continuty equations have converged.

The SIMPLE algorithm was initially developed for non-transient problems, and as a result one has to make some adjustments to it for it to be used with transient problems. By combining SIMPLE and PISO, it is possible to construct a new algorithm that is called **PIMPLE**. This algorithm is one of the most common ones for transient problems in OpenFOAM and has the advantage that it can handle large Courant numbers, which in turn makes it possible to use larger timesteps. [15]

2.8 Turbulence Modeling

In the Navier-Stokes equations in previous sections, no consideration has been taken to whether the flow is laminar or turbulent. While the characteristic of fluid flows can generally be estimated by studying the Reynolds number, the presence of turbulence adds a great deal of complexity to the field of fluid dynamics. Turbulent flow is in itself very complex and is described as a chaotic flow comprised of eddies of various sizes that rapidly mixes the fluid. Large eddies breaks down over time into smaller eddies and the energy of the turbulence dissipates into other forms such as heat. [13]

What sort of model that is used to approximate the effects of turbulence is a big part of setting up a CFD model. In general, there is a trade off for turbulence models between the resolution of the eddies calculated, and the computational power required to solve the system of algebraic equations. For some problems it is not necessary to study the finest details of the flow, and it is sufficient to use statistical quantities such as averages and standard deviations to approximate the turbulence. For other applications, the actual eddies need to be resolved numerically. The eddies can be solved for different time and length scales.

One of the common statistical methods is **RANS** (Reynolds-averaged Navier–Stokes equations). RANS predicts directly the average flow and the effects of turbulence on the mean flow. It does not resolve any turbulent eddies numerically and is therefore not that computationally expensive. RANS decomposes the flow into mean and fluctuating components:

$$\phi = \langle \phi \rangle + \phi' \tag{21}$$

with the time averaging done according to:

$$\langle \phi \rangle = \frac{1}{T} \int_T \phi \ \mathrm{dt} \tag{22}$$

and the fluctation:

$$\phi'^2 = \frac{1}{T} \int_T (\phi - \langle \phi \rangle)^2 \ \mathrm{dt} \tag{23}$$

the above equations are used with the governing equations to arrive at the Reynolds Averaged Navier Stokes equations. When doing so, it is important to notice that compared to the original equations, the equations that are derived using averaging will contain extra terms, and the equations are *open*. These terms needs to be modelled to solve what is called the *closure problem*. It has been mentioned that the RANS method does not truly resolve the turbulent eddies. For an application such as studying the noise emitted from drag and turbulence, the RANS methods are generally not of sufficient high-fidelity. RANS is better suited for more "standard" engineering studies.

A method that does not rely on averaging is **LES** (Large eddy simulation). LES does compute the eddies for the problem but the advantage of LES is that not all length scales are computed. As the name implies, LES uses a filtering function $G(\mathbf{x}, \mathbf{x}', \Delta)$, which can be seen as a low pass filter, only computing the eddies of a width larger than Δ. [12] For certain studies, the contributions of the large eddies on factors like lift and drag forces on a body, is enough to consider as these eddies carry most of the momentum. Not only are the smallest length-scales not always relevant, but calculating these require significantly more computing power than just focusing on the larger eddies. This makes LES an attractive method with a good trade off between resolution and computing power. The amount of computing power that is needed depends on the Reynolds number. A higher Reynolds number results in a wider range of length scales, requiring bigger computational

effort to be resolved.

In some applications there are only specific regions in the domain where there is a need for a detailed model like LES. When this is the case a **hybrid** turbulence model can be used. These models often combine RANS and LES, switching model in different regions depending on the flow conditions, and thereby cutting down on the computational cost. One such model is the Spalart-Allmaras Delayed Detached Eddy Simulation (DDES).

The most computationally costly method for simulating turbulence is **DNS** (Direct Numerical Simulation). DNS is fully numerical method to solve the turbulent flow and unlikey LES, it computes even the smallest length-scales. However, due to the intense computational cost, DNS cannot currently be used in wide spread industrial applications. [16] The time it takes to complete a simulation with DNS depends on the Reynolds number, but it might be orders of magnitude longer than with LES. If a simulation with LES takes weeks, it might take months with DNS.

2.9 Aeroacoustic Analogy

It is empirically known that turbulent flows and aerodynamic forces acting on surfaces generates sound. It is less obvious how this sound generation occurs, expressed mathematically. In 1952 James Lighthill published the Lighthill Analogy which is the most common aeroacoustic analogy. [17] The Lighthill analogy is a way of estimating the sound generated by modelling the sound field as a product of acoustic quadrupoles. Lighthill based his theory on a derivation of the equations of motion of a gas, into a wave like equation. Or more specifically, the sound propagation of a medium at rest. Lighthill showed that the exact equations could be written as:

$$\frac{\partial^2 \rho}{\partial t^2} - a_0^2 \nabla^2 \rho = \frac{\partial^2}{\partial x_i \partial x_j}(T_{ij}) \tag{24}$$

$$T_{ij} = \rho v_i v_j + p_{ij} - a_0^2 \rho \delta_{ij} \tag{25}$$

where ρ = density, p_{ij} = compressive stress tensor, a_0 = velocity of sound in a fluid at rest and v_i = component of velocity in direction x_i. The equations were solved on the form:

$$\rho - \rho_0 = \frac{1}{4\pi a_0^2} \frac{\partial^2}{\partial x_i \partial x_j} \int_v \frac{T_{ij}(\mathbf{y}, t - \frac{|x-y|}{a_0})}{|x-y|} d\mathbf{y} \tag{26}$$

Although his aeroacoustic analogy is the most commonly used today, others have expanded upon it since it's publication. One thing that Lighthill did not account for is the effect of hard surfaces – Lighthill only considered a free flow, and therefore the effect of reflection and diffraction is neglected. One analogy that does consider hard surfaces is the *Curle Analogy*, which was published in 1955 by Samuel Newby Curle, and is based on the Lighthill analogy. [18] The original Lighthill equations are quite lengthy, but can in many cases be simplified. This is also the case for the Curle analogy. In the CFD software OpenFOAM, Curle's analogy is implemented as simply:

$$p' = \frac{1}{4\pi}\frac{\mathbf{r}}{|\mathbf{r}|^2} \cdot (\frac{\mathbf{F}}{|r|} + \frac{1}{a_0}\frac{d\mathbf{F}}{dt}) \tag{27}$$

where p' = Curle's acoustic pressure, a_0 = reference speed of sound, $\mathbf{r}$ = distance vector to observer locations, $\mathbf{F}$ = surface normal pressure force, and t = time. Other acoustic analogies exist that also predict noise of solid walls. One is the FWH formulation (from Ffowcs Williams and Hawkings) that builds on the Curle analogy and offers one advantage over Curle – it handles flows with moving walls, compared to the Curle analogy that only handles stationary walls. [19]

3 Method

The first part of the thesis project consisted of a short literature study on the topic of propeller and wing noise emissions. Academic papers were read and collected in the program Mendeley. A portion of time was also dedicated for the author to get familiar with the software that was to be used. After discussing with his supervisor, it was decided that the program OpenFOAM on Linux was appropriate for the project. OpenFOAM has no graphical user interface, but instead runs in a shell environment. This takes some time to learn, especially without prior experience. To practice using OpenFOAM, the tutorials were studied.

3.1 Creating a Computer Model of the Propeller

After getting familiar with Linux and OpenFOAM, the next step was to create a computer model of the drone propeller that was to be used. The propeller manufacturer *APC Propellers* has since long specialised in producing propellers for SUAV's. The company had a propeller available called *4.1 x 4.1 E* which is a propeller with a propeller diameter of 4.1 inches (10.4 cm) made for electric vehicles. Upon request, the company graciously shared the full geometrical and technical data sheet of the propeller, which made it possible to create a computer model of the propeller in the program Solidworks. The propeller profile was based on an E63 airfoil. Using an airfoil tool containing standard airfoils such as the E63, cross sectional curves were generated for the propeller. These cross sections, spanning the radius of the propeller, were then imported into the CAD program Solidworks. Using the geometry data provided by the manufacturer these curves were then arranged so that a wing structure could be created with the Loft feature (see Figure 3).

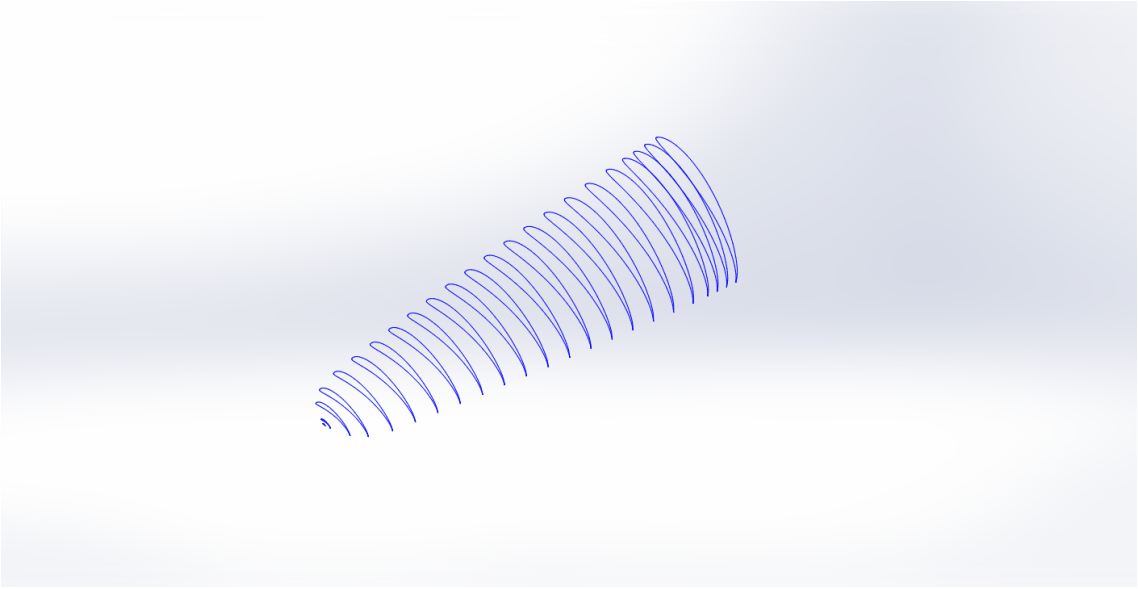

Figure 3: Individual Airfoil Cross Sections

The wing that was created was then supplemented as closely as possible to the original, with additional features such as hub and hub transition. The final result can be seen in Figure 4, in which the cross sectional airfoils are left visible in one half of the propeller.

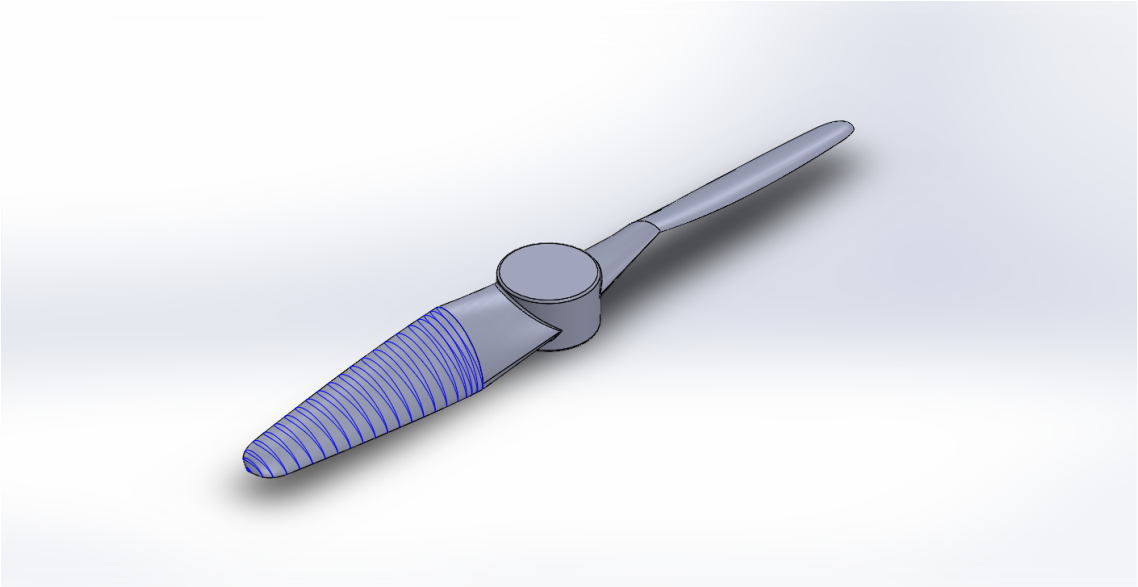

Figure 4: Complete Initial Propeller Model

3.2 Modifying the Original Propeller

With the original propeller constructed into a usable 3D format it was time to make the first modifications to the design. Since the noise emitted from the propeller is effected to a large degree of the vortices generated from the trailing edge, it seemed like a good idea to initially modify the trailing edge of the propeller. This modification not only makes sense in light of the existing research on propeller noise, referenced under the the *theory* section, but also resembled the structure that can be seen in nature on some bird's wings. Nature has had millions of years to perfect its engineering solutions via evolution and it makes a lot of sense to look at nature for inspiration. The profile on the trailing edge of an owl's wing does not follow any obvious regular pattern or function. Therefore a design choice was made to simplify the modification and to instead use a mathematically driven design. The design was a simple triangular wave pattern along part of the trailing edge. An advantage with a mathematical pattern like this one is that it is per definition quantified and can therefore easily be parameterised, simplifying engineering optimization. The design can be viewed in Figures 5 and 6.

The propeller wing tip speed is a large contributor to the noise generated by a propeller and therefore it makes sense to try a modification that only aims at minimising the vortices created at the wing tip. Furthermore, designs like these – only present at the tip of the propeller at the trailing edge – has proven to be efficient in previous studies. [20]
The working principle of the serrations is to reduce the large scale vortex structures that are generated at the trailing edge. The sharp tips of the triangular and sinus shapes helps to break these vortices into smaller smaller vortex structures [21]. As previously discussed, these vortices are a main source of the noise that is generated. The triangular wave has a sharper tip which might break up vortices differently than the sinusoidal wave. It probably also easier to manufacture. One downside could be that sharp corners can be prone to crack propagation.

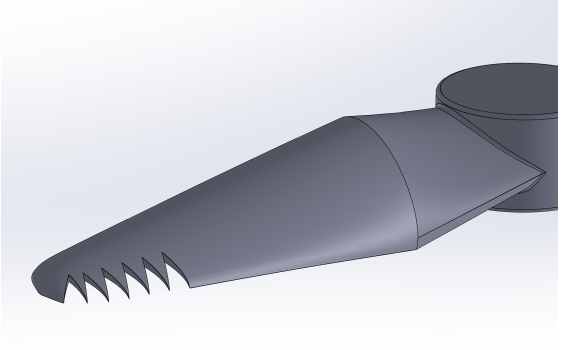

Figure 5: Propeller With Triangular Cutaway at the Outer Third

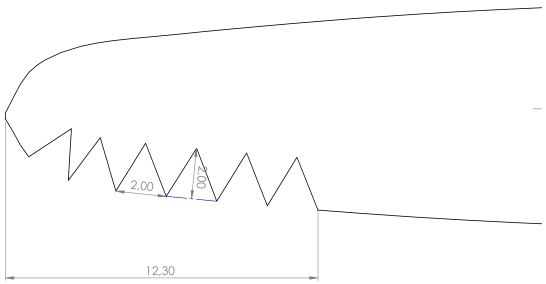

Figure 6: Drawing of propeller with Triangular Cutaway

In addition to the triangular wave pattern, other designs were experimented with too. These designs were also mathematical and consisted of a sinusoidal wave pattern. The sinusoidal design was used both along the entire trailing edge and also just at the outer radius of the propeller, resulting in two designs. These designs can be seen in Figures 7 & 8 and in Figures 9 & 10.

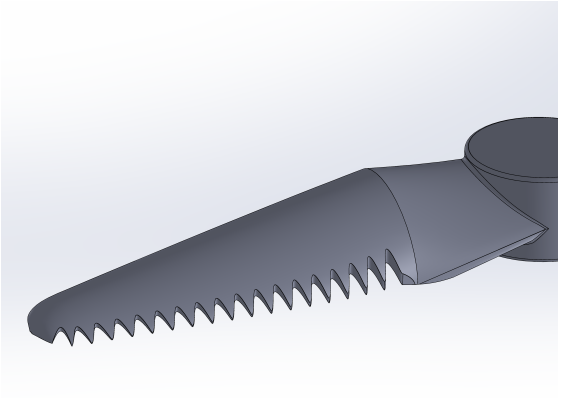

Figure 7: Propeller with Sinusoidal Cutaway Along Entire Trailing Edge

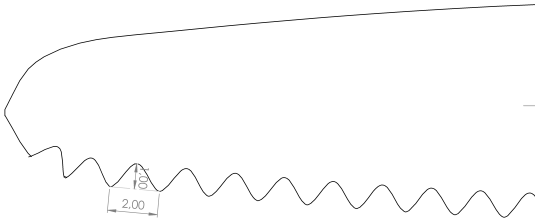

Figure 8: Drawing of the Sinusodal Cutaway

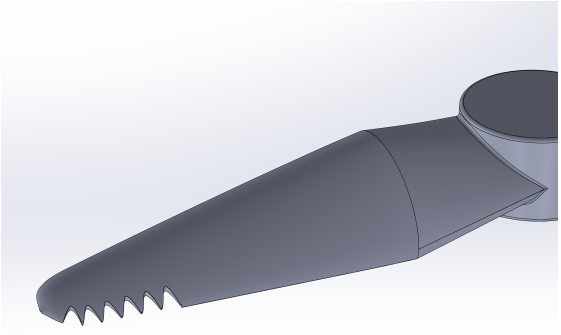

Figure 9: Propeller with Sinusoidal Cutaway at Outer Third

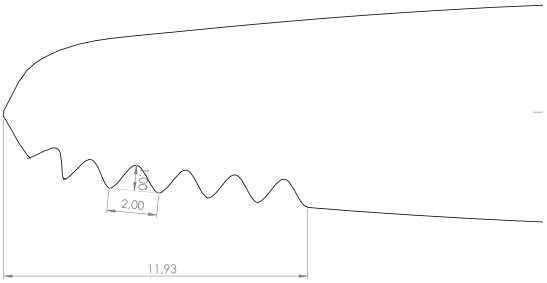

Figure 10: Drawing of Sinusdoidal Cutaway

The summary of the 3 modifications can be seen in Table 1.

Table 1: Summary of the different propeller designs

Modification Version	**Type**	**Geometry**
1	Trailing Edge	Triangular Cutaway Outer Third
2	Trailing Edge	Sinusoidal Cutaway
3	Trailing Edge	Sinusoidal Cutaway Outer Third

3.3 Meshing and Strategies for Rotating Geometry

Meshing for the different propellers was done in OpenFOAM using cfMesh.

cfMesh generates a mainly hexa-dominated octree refined mesh with polyhedral cells close to the surfaces.

This is suitable for more complex geometries. Many of the propellers that were to be evaluated had intricate parts – mainly along the trailing edge – and it would not have been possible to generate a mesh for these geometries that was structured.

Due to the special interest in the very small vortices generated by the trailing edge of the propellers, and also since the modifications on the propeller edges was made out of patterns that were the size of a few millimeters, it was necessary to insert local refinements. Without these the alternative would have been to use a smaller mesh size for the entire propeller geometry and this would have significantly slowed down the computations. The maximum cell size for the domain and at the domain boundaries was set to 0.075m. To achieve a smaller cell size for the propeller, 8 levels of local refinements were inserted. That means that the cells in that area are smaller than on the coarsest level with a factor 2^8. The refinement thickness was set to 0.001m. In addition to the local refinements, 5 boundary layers were inserted around the propeller in order to resolve the higher velocity gradients around the propeller walls. The mesh can be seen further down in the subsection *Final Mesh*.

The presence of rotating components poses an extra challenge to a CFD problem and there are multiple ways to setup a case. One of strategies is to use a single rotating frame, often abbreviated **SRF**. Like the name implies, SRF uses a single rotating frame to compute the fluid flow, in a frame of reference that adheres to the rotating geometry. OpenFOAM offers SRF solver that uses either the SIMPLE or the PIMPLE algorithm. Another way to setup the case with rotating geometry is to use multiple reference frames, or **MRF**. MRF uses the rotating frame that is found in SRF and in addition uses an outer stationary frame that encompasses the inner frame. The MRF model is commonly used in applications with mixing tanks, where the mixing performance of a inner rotor on an outer "stationary" fluid is to be evaluated. For studying the turbulent eddies generated by a rotating propeller, using the SRF model was deemed sufficient. Especially since the region outside the proximity of propeller was not really of any interest. Thankfully so, since with SRF it can be a challenge to get a realistic simulation at the outer radius when there is a frame with a large radius or a high rpm. This is due to the artificial centrifugal force that is generated by the rotation. Beside SRF and MRF, it would have been possible to use a *dynamic mesh* with an OpenFOAM solver like `pimpleDyMFoam`. A drawback with dynamic meshes is however that there is an increase in computational cost. [22]

3.4 OpenFOAM Setup

The simulations in the project was done using two main OpenFOAM setups.

3.4.1 Setup 1

The first group of simulations was done using a rotational mesh structure with a single rotating frame, containing the geometry of interest inside, which is the propeller. The SRF was suitable to simulate the interaction between the propeller and the air around it during rotation. The rotating frame with the small basic propeller (in green) in the middle, can be seen in Figure 11

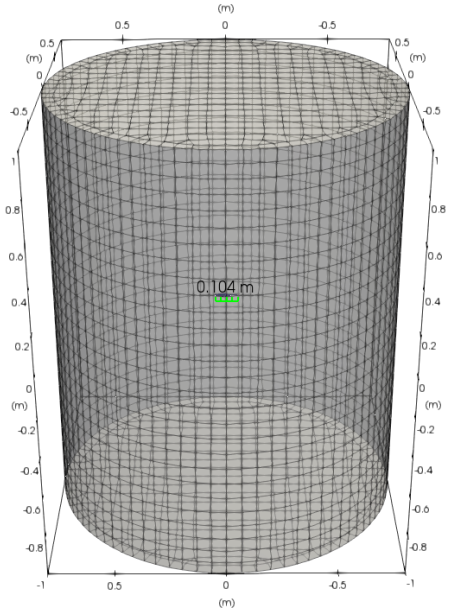

Figure 11: Rotating Mesh Frame

A summary of the main settings of the OpenFOAM setup can be seen in Table 2. OpenFOAM with its open source environment offers great flexibility and it is possible to control most settings down to minute details. Therefore the settings in 2 are not a complete overview of all of the settings.

Table 2: Summary of the case setup in OpenFOAM

Application	SRFPimpleFoam
Turbulence Model	
Type	LES
LES type	SpalartAllmarasDDES
Transport Model	Newtonian
SRF Model	
Type	RPM
RPM Coefficient	-3600
Boundary Conditions	
Rotor	Wall, No-Slip
Top	Wall, Rotating Wall Velocity
Side	Wall, Rotating Wall Velocity
Bottom	Wall, Rotating Wall Velocity
Timestep	1e-05 s

The turbulence model of choice was LES, in order to capture the small eddies and pressure differences involved in noise generated. The type SpalartAllmarasDDES is suitable for predicting turbulent flow of processes with high Reynolds numbers, which drone propellers have. This can easily be understood by looking at the rpm of the propeller. Some quick simulations using the WALE LES model were performed too. These showed no significant improvement compared to SpalartAllmarasDDES so the simulations proceeded using only SpalartAllmarasDDES. The transport model is Newtonian which assumes constant fluid viscosity ν. The OpenFOAM case uses the fluid air and a kinematic viscosity of $\nu = 1.5 \cdot 10^{-5}$ m^2/s . The RPM value for the rotating frame was set to -3600 revolutions per minute (rpm). The choice of 3600 rpm was relatively arbitrary. There are commercial drones on the market today with an operating rpm of everything from 2000 to 9000 rpm. While researching drones there was some popular drones from DJI that had a propeller rpm of 3600 while in stationary flight and therefore that value was used. The boundary conditions used was "Wall" for all surfaces such as the rotor surface and the surfaces of the rotating frame. This choice assumes that the rotating frame or domain is large enough so that any air displaced by the propeller does not affect the vortexes or pressure fields around it, even though the air cannot cross the domain boundaries.

3.5 Setup for Post-Processing

In OpenFOAM the data that is to be generated from the simulations needs to be specified. For the purpose of evaluating propellers, some data of interest is the forces acting on them. This is to make sure that any modifications to the propeller geometry does not render the propeller useless in terms of flight properties. For the noise evaluation, it is of interest to study the vortices generated by the propeller. This can be done by inserting probes into the solution domain that monitors the pressure.

The probes that are inserted are fixed in the domain thus they rotate with the same speed as the rotor. This is advantageous since the probes can then easily simulate following behind the propeller at a fixed distance. Taking this into consideration, the post-processing settings were chosen as seen in Table 3.

Table 3: Post-Processing specification in OpenFOAM.

Forces	
Propeller Forces	$F_x, F_y, F_z, M_x, M_y, M_z$
Probes	
Number of Probes	2
Fields	p, U
Locations	(0.01 0.04 0.0) (0.01 0.04 -0.01)

The base propeller with the probes visible can be seen in Figure 12.

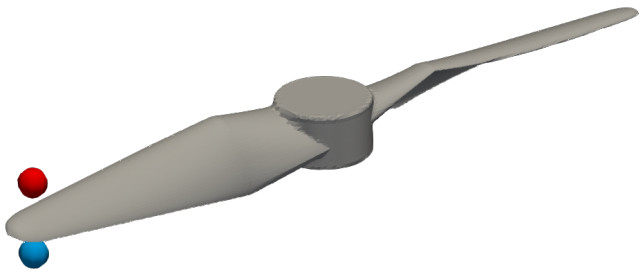

Figure 12: Propeller with probes represented in red and blue.

The data that was generated from the simulations was then analysed using the programming language Python with some common libraries such as NumPy.

3.6 Mesh Sensitivity Analysis

The final mesh cell size used for the domain was arrived at by conducting a mesh sensitivity analysis. A mesh sensitivity analysis is a way of determining an appropriate mesh cell size. This is important because there is trade-off between the precision of the converged solution and the computational requirements to run the simulation. With a simulation such as the one used in this project that uses an LES turbulence model, there is much computational time to be saved by using a sufficient number of cells and not more. For the mesh analysis, three different meshes were used. These were called *Coarse*, *Medium* and *Fine*. The mesh for all of these were setup as described in the meshing section. The difference between them was the maximum cell size and the number of cells. These differences can be seen in Table 4.

Table 4: The three meshes used for the mesh sensitivity analysis

Mesh	**Coarse**	**Medium**	**Fine**
Max cell size [m]	0.100	0.075	0.055
Number of cells	$1.48 \cdot 10^6$	$3.59 \cdot 10^6$	$8.89 \cdot 10^6$

The case that was used to conduct the mesh sensitivity analysis was Case 1 that has previously been described. The simulations for the three meshes were run for a relatively short period of time and then some main characteristics were studied. The chosen data for study was the propeller lift force and the pressure from the probes. A diagram of the lift forces can be seen in Figure 13. The forces are smoothed with a running average and are not instantaneous.

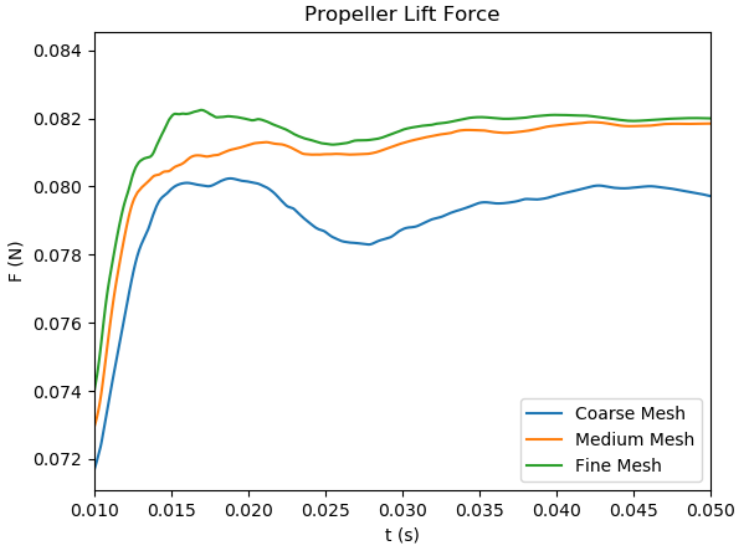

Figure 13: Diagram of the Smoothed Lift Forces as a function of Time from Propeller Start

It can be seen that the coarse mesh stands out with its lower propeller lift force. Between the medium and the fine mesh, the difference is smaller. The differences between the three meshes, summarised in a diagram with the lift force as a function of mesh cell count, can be seen in Figure 14:

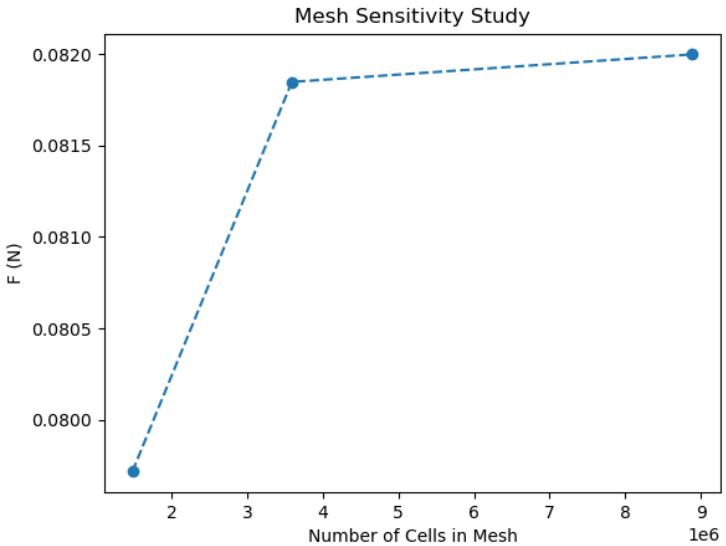

Figure 14: Lift Force as a Function of Mesh Cell Count

Looking at Figure 14 it can be seen that increasing the number of cells more than the amount in the medium mesh, does not seem to yield a significantly better result. Doing so would however increase the computational time. With the LES turbulence model, the computations are already

quite slow. That is the reason why these initials mesh simulations are only run for a short period of time. Normally the solution should be fully converged, but this would have taken far to long time in these cases. The solutions in Figure 13 were deemed sufficiently converged.

The vertical velocity component from the probe located under the propeller – probe 2 – was also studied. The result of this study can be seen in Figure 15. Once again the difference between the fine and the medium mesh is not as large as the difference between the coarse the other two meshes. This time there is however a small inconsistency in that the medium mesh yields a higher velocity component than the fine mesh. This difference is however relatively small.

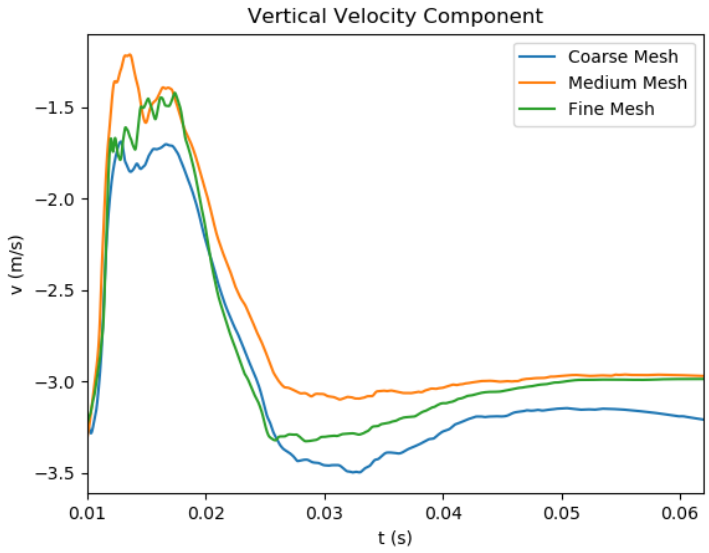

Figure 15: Vertical Velocity Component of Probe 2

The vertical velocity component as a function of mesh cell count can be seen in Figure 16

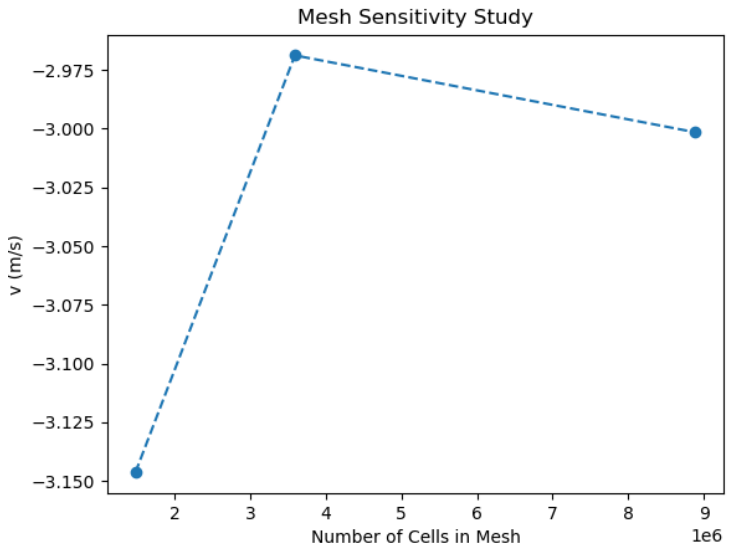

Figure 16: Vertical Velocity Component as a Function of Mesh Cell Count

After comparing the different mesh sizes and the resulting lift forces and velocity component values, the choice fell on the *medium* mesh. Despite the small inconsistency in the vertical velocity component from probe 2, the mesh size of the medium mesh resulted in a solution valued that was

good enough. Using the finer mesh would have resulted in diminishing returns and a far greater computational burden.

3.6.1 Final Mesh

The final mesh for the first case can be seen below. Figure 17 and 18 shows cross sections of the rotating frame, with the local mesh refinements around the propeller. Figure 19 shows a closer look at the propeller in the cross sectional view. Due to the the exponentially growing number of cells in the refinement areas, the cell lines obscures some of full mesh cell visibility. In Figure 20 the propeller is visible, with the local mesh cell refinements along the trailing edge, discussed in the meshing section.

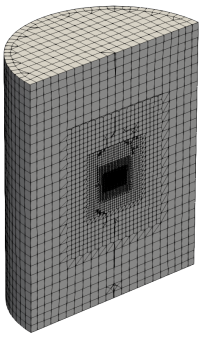

Figure 17: Vertical Cross Section of Mesh

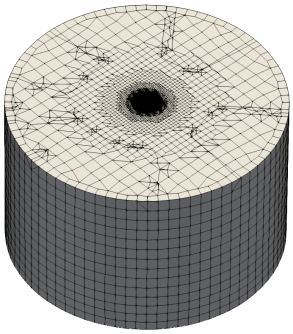

Figure 18: Horizontal Cross Section of Mesh

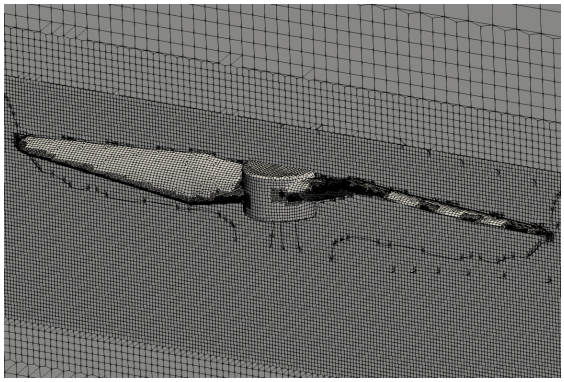

Figure 19: Propeller in the Rotating Frame

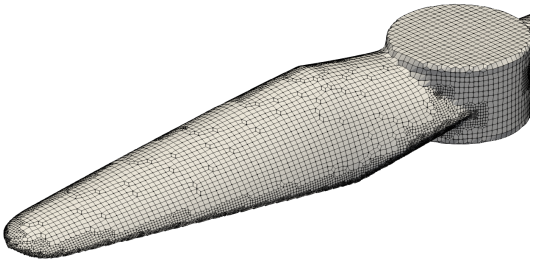

Figure 20: Propeller with Trailing Edge Refinements Visible

3.7 Case 2

The second case was setup due to some unexpected limitations in the version of OpenFOAM that was being used. The simulations for case 1 was done using OpenFOAM version 9. That version does not offer any acoustic solver that implements Lighthill's acoustic analogy. Since this was of importance to the field of study, OpenFOAM v2106 was used instead for the second case. However, that version too has its idiosyncrasies and it was soon discovered that it was not possible to place the Curle points in the rotating frame so that they were trailing the propeller – it was only possible to have them fixed in the solution domain. Because of this the decision was made to not use a rotating frame in case 2, but instead a rectangular one. Using a non rotating case to analyse the propeller wings should be fine. The difference in Reynolds number aside, owls in nature are rarely seen rotating at 3600 rpm. The setup for the second case can be seen in the summary in Table 5.

Application	pimpleFoam
Turbulence Model	
Type	LES
LES type	Wale
Transport Model	Newtonian
Noise Model	Curle
Boundary Conditions	
Inlet Velocity	19.0 m/s
Top	Symmetry
Bottom	Symmetry
Left	Symmetry
Wall	Symmetry
Rotor	Wall
Timestep	1e-05 s

Table 5: Summary of the second case setup in OpenFOAM

In this case, the propeller was cut and placed along the left wall. The propeller hub was discarded and the only part remaining was the outer wing. Figure 21 shows an overview of the case, with the inlet represented by the red plane, the outlet represented by the blue plane and the flow field represented by the green arrows.

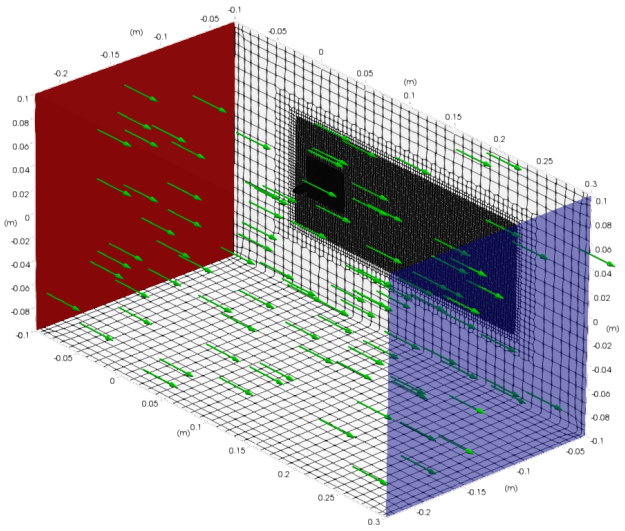

Figure 21: Overview of Case Setup

3.8 Setup for Post-Processing

The post-processing for the second case shared many similarities with the first case, but there was a greater focus on the acoustic solver and on pressure probes. The noise model calculates the noise based on the pressure in individual points, therefore it is required to specify the points in which the noise is to be calculated. The pressure probes were inserted in the near proximity of the trailing edge of the propeller wing, as seen in Figure 22 The acoustic analogy that was used was Curle's analogy due to the hard surface of the propeller and therefore Curle points were defined in OpenFOAM. These Curle Points were inserted along the x-, y-, and z-axis respectively so that they spanned the space around the propeller, making noise analysis in each direction possible. This probe distribution can be seen in Figure 23. A specification of the post-processing can be seen in table 6.

Forces	
Propeller Forces	$F_x, F_y, F_z, M_x, M_y, M_z$
Probes	
Number of Probes	10
Fields	p, U
Locations	(0.01 -0.030 0) , (0.02 -0.030 0) (0.04 -0.030 0) , (0.08 -0.030 0) (0.16 -0.030 0) , (0.01 -0.050 0) (0.02 -0.050 0) , (0.04 -0.050 0) (0.08 -0.050 0) , (0.16 -0.050 0)
Curle Points	
Number of Points	20
Locations	(0.01 -0.050 0.0) , (0.02 -0.050 0.0) (0.04 -0.050 0.0) , (0.08 -0.050 0.0) (0.16 -0.050 0.0) , (0.32 -0.050 0.0) (0.64 -0.050 0.0) , (1.28 -0.050 0.0) (-0.02 -0.050 0.0) , (-0.08 -0.050 0.0) (-0.32 -0.050 0.0) , (0.01 -0.050 0.02) (0.01 -0.050 0.08) , (0.01 -0.050 0.32) (0.01 -0.050 -0.02) , (0.01 -0.050 -0.08) (0.01 -0.050 -0.32) , (0.01 -0.100 0.00) (0.01 -0.200 0.00) , (0.01 -0.400 0.00)

Table 6:

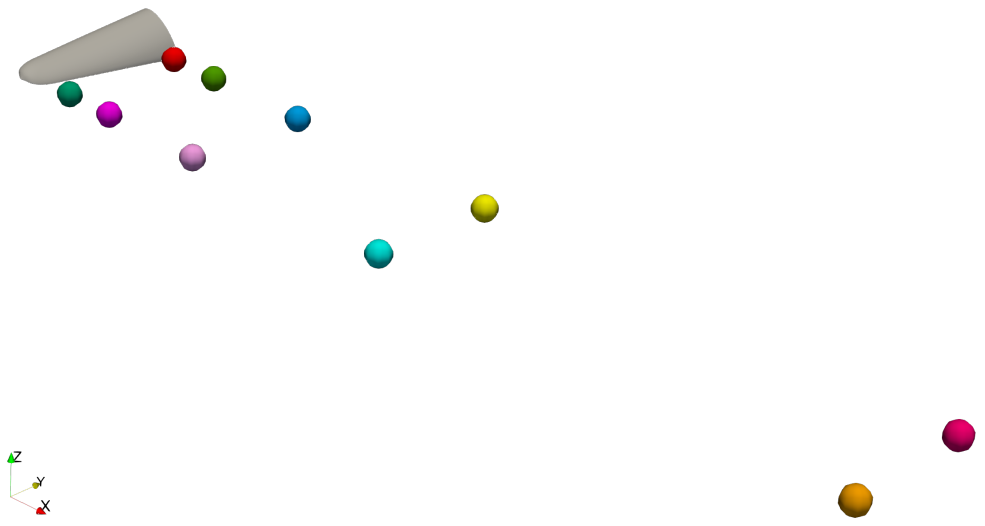

Figure 22: Probes

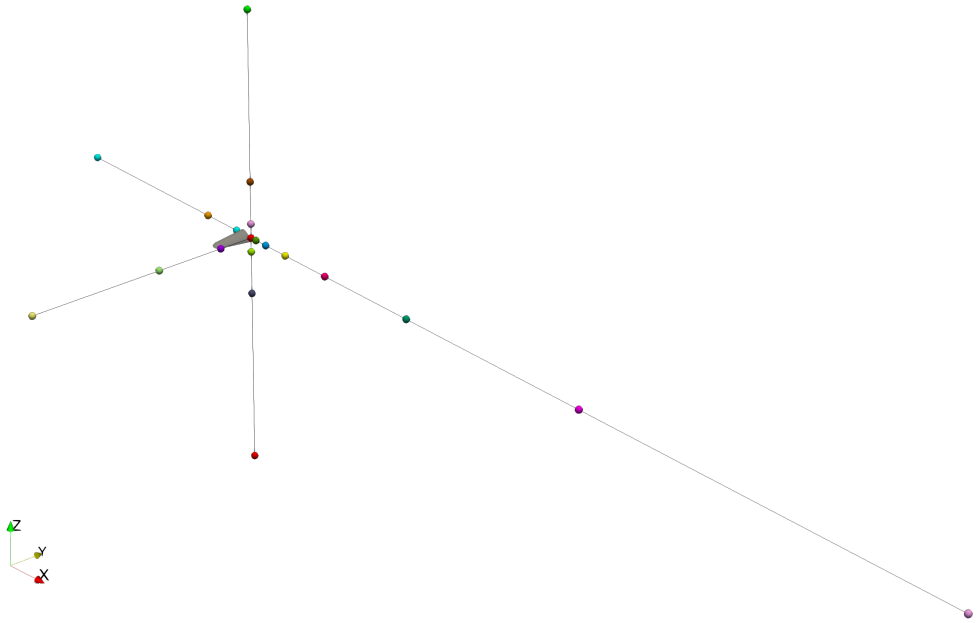

Figure 23: Curle Points

3.9 Meshing

The maximum cell size for the mesh in case 2 was 0.010m, which is smaller than in the first case. Local refinements were inserted here too – at the leading and trailing edges of the propeller wing. 5 refinement levels around the propeller were inserted, corresponding to mesh cells that are a factor 2^5 smaller in that area. The refinement thickness was set to 0.002m. For this mesh there was no mesh sensitivity analysis conducted, for several reasons. The study that was conducted on the first mesh gave a good indication of what an appropriate mesh cell size was. The second case has very similar physics compared to the first one, so it can be assumed that a mesh cell size smaller or equal to the first cell size would be sufficient. The smaller final mesh cell size choosen gives a high degree of confidence that the simulation will run fine. With the non rotating frame and the fixed inlet velocity, it will take a shorter time for the flow to be developed around the propeller than in the rotating case, which will need more time to develop the flow in the solution domain. For a figure of the final propeller mesh, see Figure 24

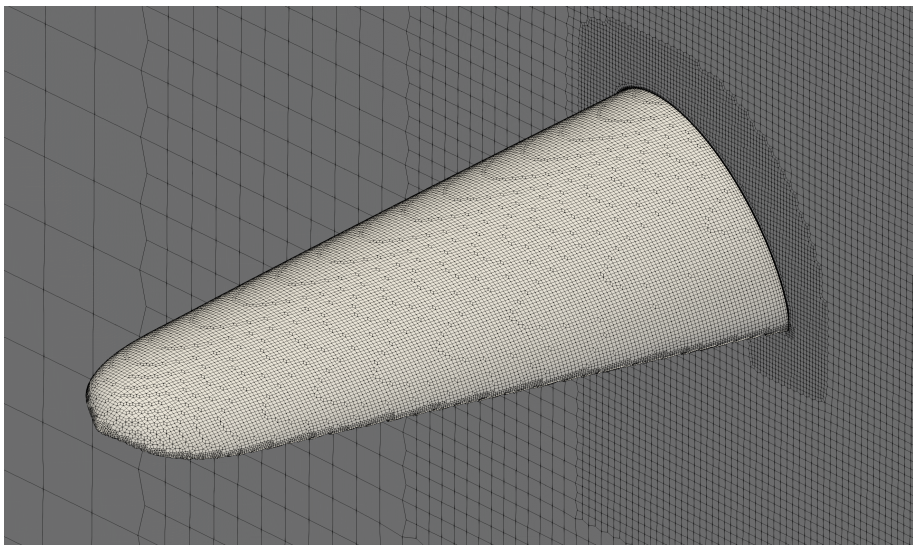

Figure 24: Mesh of the Propeller

4 Results and Discussion

4.1 Propeller Performance

It is of little use to have a silent propeller if the modifications that are made to reduce noise also negatively affect the flight properties. Therefore the propeller performance was studied to see if the modifications are viable. The main performance metric that was studied and that is arguably the most important is the propeller lift force. Lift force is dependent on wing surface area, and in all of the modifications to the wing there was a removal of wing surface area. With this in mind, it comes as no surprise that the overall lift force was lowered for the propellers the were modified. The lift force time series for the propellers can be seen in Figures 25 and 26. Figure 25 shows the lift force for the base propeller. The gray line is the momentaneous lift force and the blue line is the lift force smoothed with a running average. Figure 26 shows the lift force for all propellers, smoothed for a better overview. As expected, the propeller which had the most wing surface removed – the propeller with a sinus serration along the entire trailing edge – has the lowest lift force.

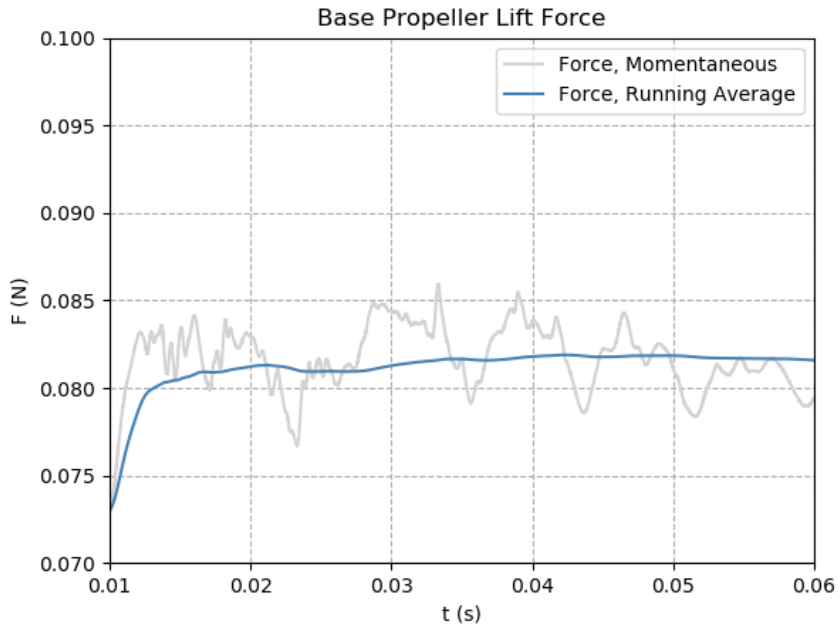

Figure 25: Momentaneous and Running Average Lift Force of the Base Propeller

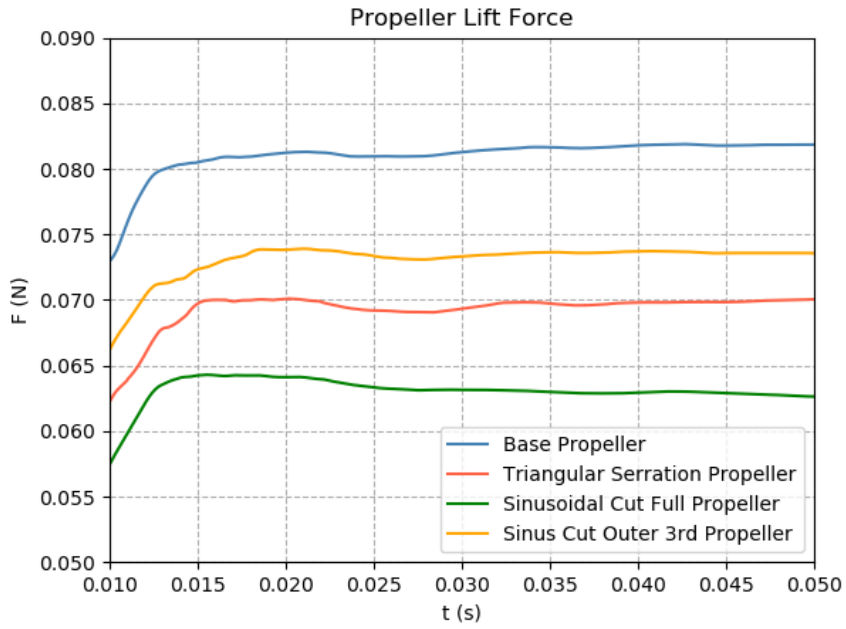

Figure 26: Running Average Lift Forces for All Propellers

4.2 Vortex Visualisation

The vortices from the trailing edge from the different propellers were studied since they are a main contributor the noise that is produced. One way to visualise the vortices and the turbulent flow structures generated in the air is to use the *Q criterion*. In OpenFOAM this is represented by the Q function which calculates the second invariant of the velocity gradient tensor. The flowfield is then visualised in Paraview. Using the Q function to generate isosurfaces (surfaces of equal Q value), visualisation for the flow field at the trailing edge of each of the four propellers were made. These can be seen in Figures 27, 28, 29 and 30. The isosurfaces in the figures below are colored by the velocity magnitude. The Q criterion offers a way to qualitatively analyse the flow fields generated, and the results are very interesting. By studying the isosurfaces generated for the unmodified base propeller, it can be seen that this propeller has clear vortices forming along the entire trailing edge, with the highest concentration – or area with highest velocity gradients – seen at around one half of the propeller radius. At the propeller wing tip the anticipated large wing tip vortex can be seen. The phenomena of large vortices at the wing tip is well known and engineering solutions to minimise these drag causing vortices have been used for many years. Therefore it is perhaps unexpected to also find the high amount of vortices in the middle of the propeller.

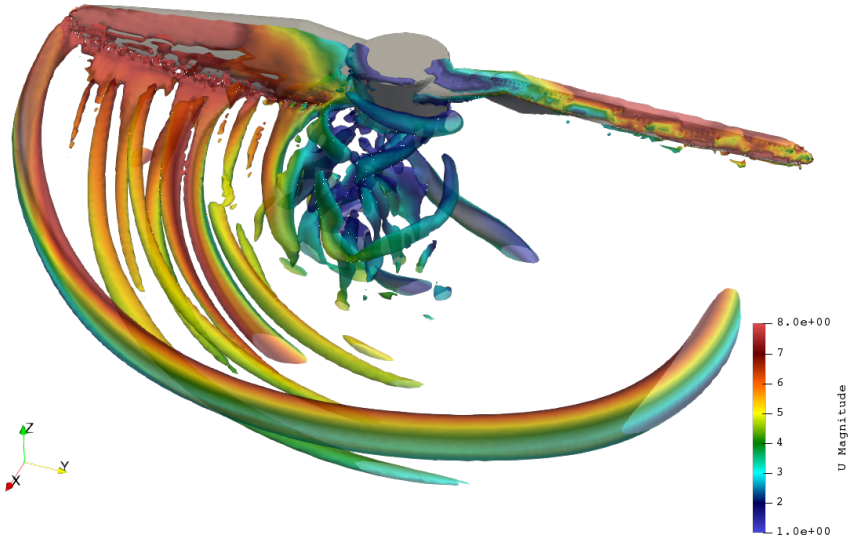

Figure 27: Base Propeller. Isosurfaces Computed at 300 000 in Paraview. Colored by Velocity Magnitude.

Moving on to the propeller with a sinusoidal modification to the outer third, seen in Figure 28 the results here are also interesting. There appears to be an ever so slight reduction of vortices along the length of the propeller which has been modified. However, neither the big vortex at the wing tip or the concentrated area in the middle of the wing radius has been effected of the modification. The purpose of only modifying the outer area of the wing was to target the vortices known to occur at the tip, but instead this modification falls short.

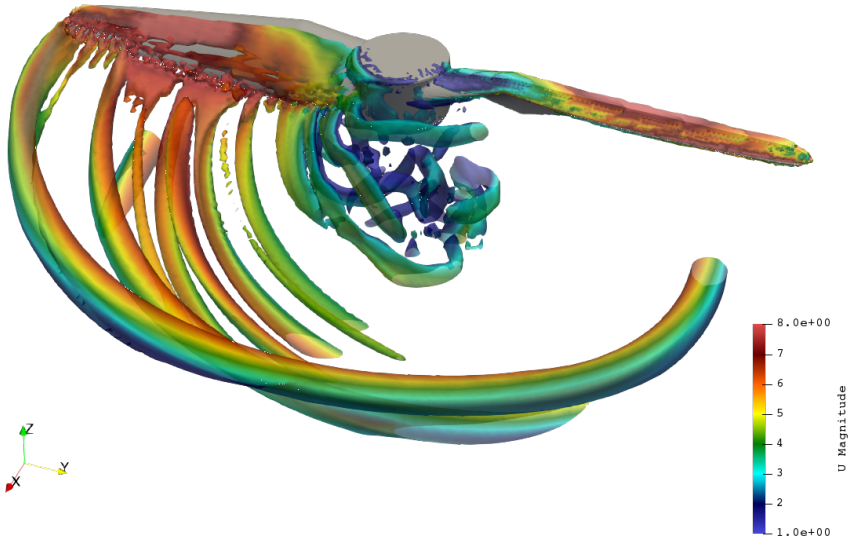

Figure 28: Sinus 3rd Propeller. Isosurfaces Computed at 300 000 in Paraview. Colored by Velocity Magnitude.

The modification of a triangular cutaway also falls short. Both figuratively and literally. The modification does not seem to have a large effect of neither the propeller tip vortex or the concentrated vortex area in the middle. The length of the modification simply seems to be too *short*, or

misplaced. Compared to the previous modification, the triangular modification does not seem to offer any improvement.

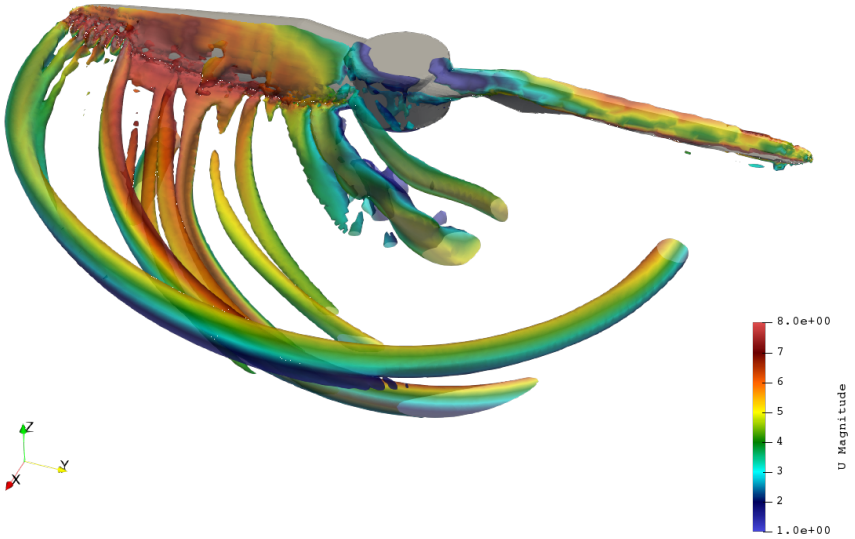

Figure 29: Triangular Cutaway Propeller. Isosurfaces Computed at 300 000 in Paraview. Colored by Velocity Magnitude.

The final propeller which had a modification of a sinusoidal cutaway along the entire trailing does show promising results. The modification does not seem to short this time and by looking at the isosurfaces, and by comparing to the other propellers, there actually seems to be a significant reduction of vortexes generated along the trailing edge. The large wing tip vortex is however still present.

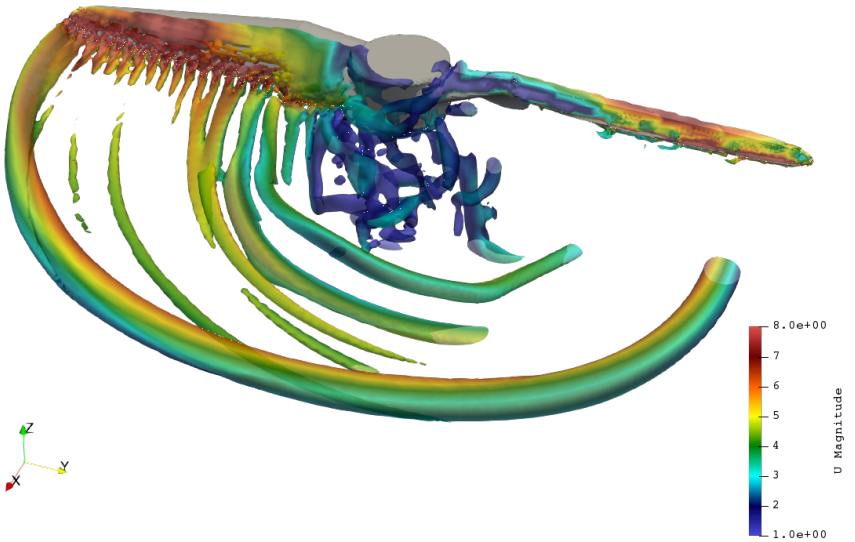

Figure 30: Full Sinus Serration Propeller. Isosurfaces Computed at 300 000 in Paraview. Colored by Velocity Magnitude.

It is not really possible to completely eliminate the wing tip vortex. Something that is possible though is to introduce small fluctuations close to it that breaks it down faster, something the

serrations should do to variyng degrees. In the figures above it is hard to get an overview of how the wing tip vortex is broken down, due to the choice of value for the isosurfaces. Therefore, isosurfaces with a higher Q value, that filters out smaller vortices are shown below in Figures 31, 32, 33 and 34. The Q values of these isosurfaces are $5 \cdot 10^6$ and they are also colored by velocity magnitude.

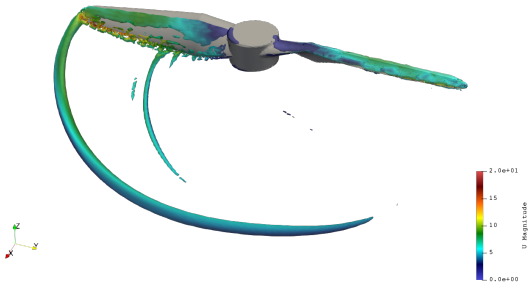

Figure 31: Base Propeller

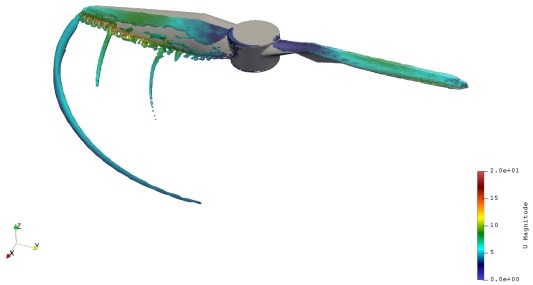

Figure 32: Sinus 3rd Propeller

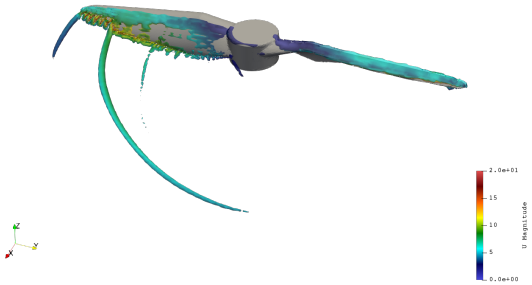

Figure 33: Triangular Cutaway Propeller

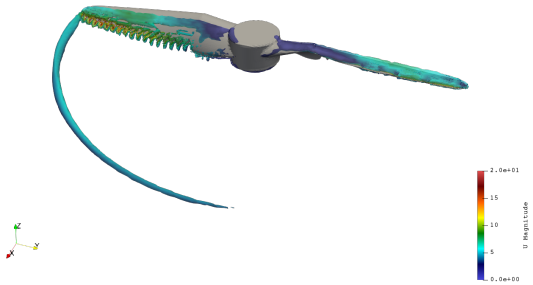

Figure 34: Full Sinus Serration Propeller

From this point of view it appears that the modified propellers do show wing tip vortices that dissipates faster than the unmodified base propeller.

4.3 Spectral Analysis

The propellers can and should also be analysed in a quantitative manner. Using the pressure probes described in the case setup the pressure level was calculated. A Fourier analysis was then performed to study the pressure level signal in the frequency domain. The Fourier analysis reveals that the spectrum is comprised both of tonal noise as well as a broadband noise component. Although "noise" is mentioned, it should be clarified that the pressure probes in the case setup can only really logg the hydrodynamic pressure in incompressible flow and not actually the sound. Due to the relationship between pressure and sound, the pressure spectrum is sometimes referred to as "noise" in this section. The noise characteristic of the base propeller shows this broadband noise in the higher frequencies, along with what appears to be tonal noise in the lower frequencies. The tonal noise seems to be at the blade pass frequency of $f_{bpf} = 120$ Hz and the corresponding harmonics, found at $f_{bpf} \cdot$n. The base propeller appears to have loud harmonics of the blade pass frequency at $f = 600$ Hz and $f = 1200$ Hz, which are represented in Figure 35 with vertical red dashed lines.

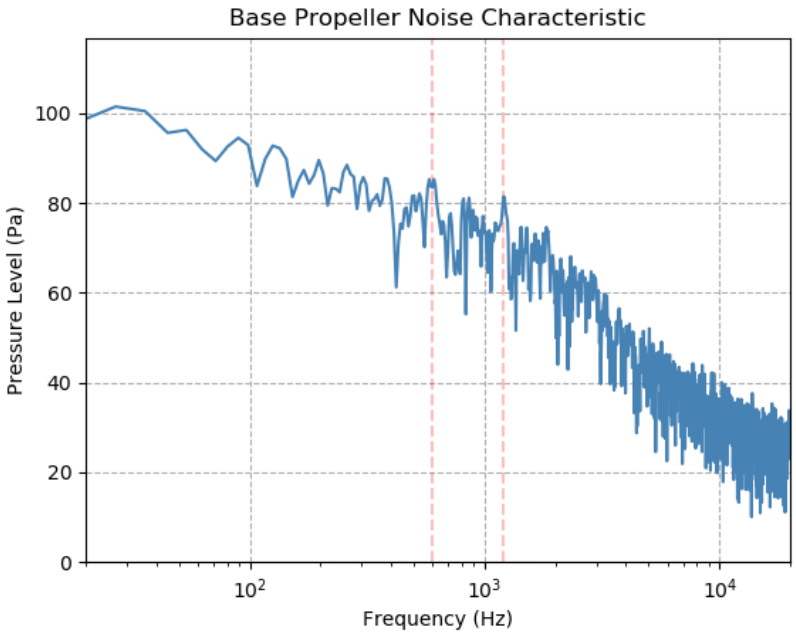

Figure 35: Pressure Spectrum of the Base Propeller. Vertical Red Lines at $f = 600$ Hz and $f = 1200$ Hz

The propeller with the sinusoidal serration at the outer radius also shows broadband fluctuation components at the higher frequencies. This propeller shows strong tonal noise components at the harmonics of the blade pass frequency. In Figure 36 the frequencies of $f = 120$ Hz, $f = 240$ Hz, $f = 480$ Hz and $f = 840$ Hz are represented with vertical red dashed lines. The ISO surfaces of the previous section showed that the modification was of little use and the spectral analysis confirms it.

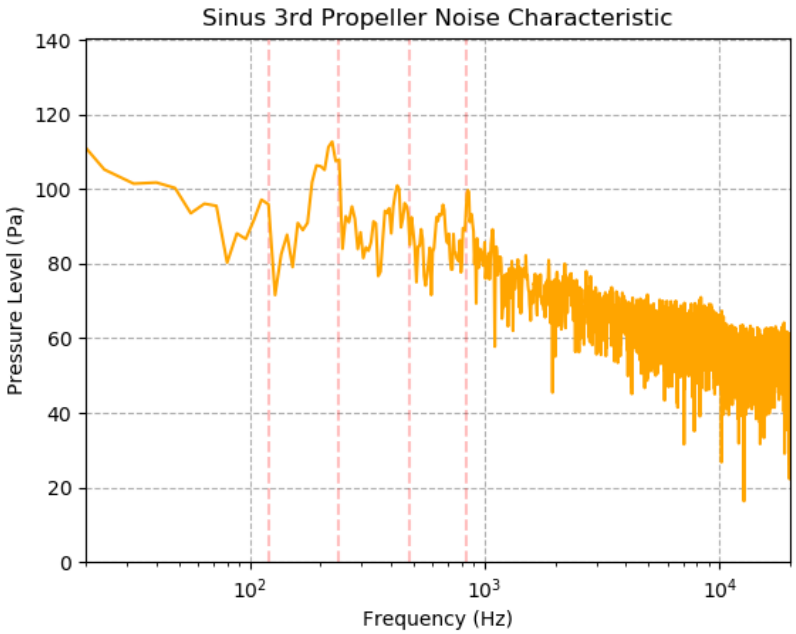

Figure 36: Pressure Spectrum of the Sinus 3rd Propeller. Vertical Red Lines at $f = 120$ Hz, $f = 240$ Hz, $f = 480$ Hz and $f = 840$ Hz

The propeller with the full sinusoidal serration appears to have a noise characteristic that

matches the result in the vortex visualisation. Except for a tonal noise at twice the f_{bpf} = of 240 Hz there is not much but a broadband noise revealed by the spectral analysis.

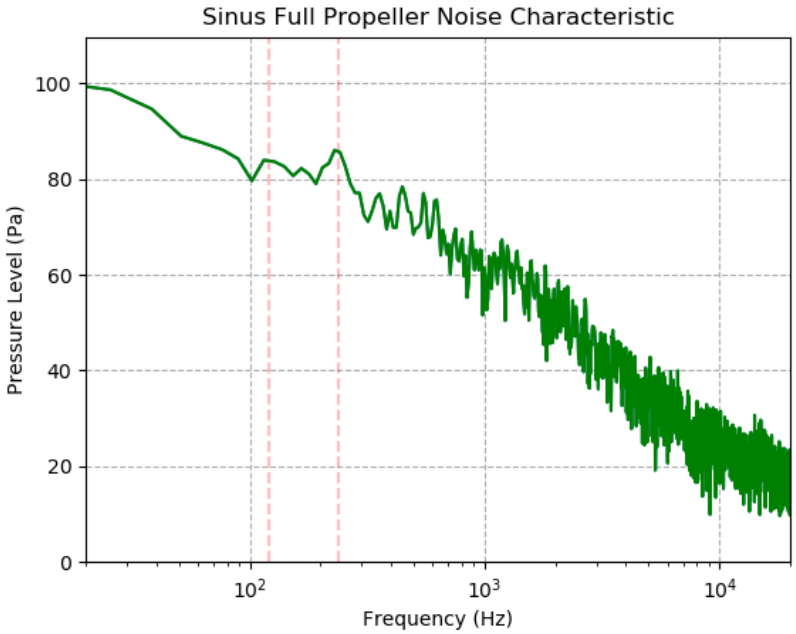

Figure 37: Pressure Spectrum of the Sinus Full Serration Propeller. Vertical Red Lines at $f = 240$ Hz

Lastly there is the triangular cutaway modification propeller which surprisingly does not seem to share characteristics with the poorly performing second propeller of the spectral analysis. This propeller appears to have a tonal component at 720 Hz, marked with a vertical red dashed line in 38.

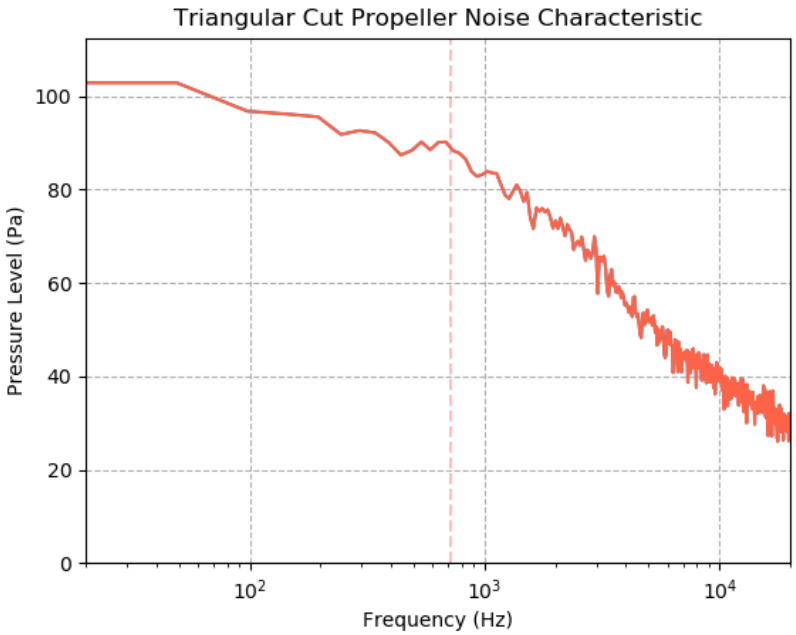

Figure 38: Pressure Spectrum of the Triangular Cut Propeller. Vertical Red Lines at $f = 720$ Hz

As a way of comparing the noise characteristic of the four propellers they are plotted in 39 using a smoothing moving average of length 30. From this comparison it appears that the propeller with

the full sinusoidal cutaway and the triangular cutaway shows a quieter noise characteristic than the unmodified propeller. The propeller with the Sinus 3rd modification stands out with its much louder noise characteristics, a performance that is so poor and so vastly different to the similar triangular cutwaway, and the other propellers, that it is likely that there is a problem with the Fourier transform that has been made, or some numerical error in the simulation.

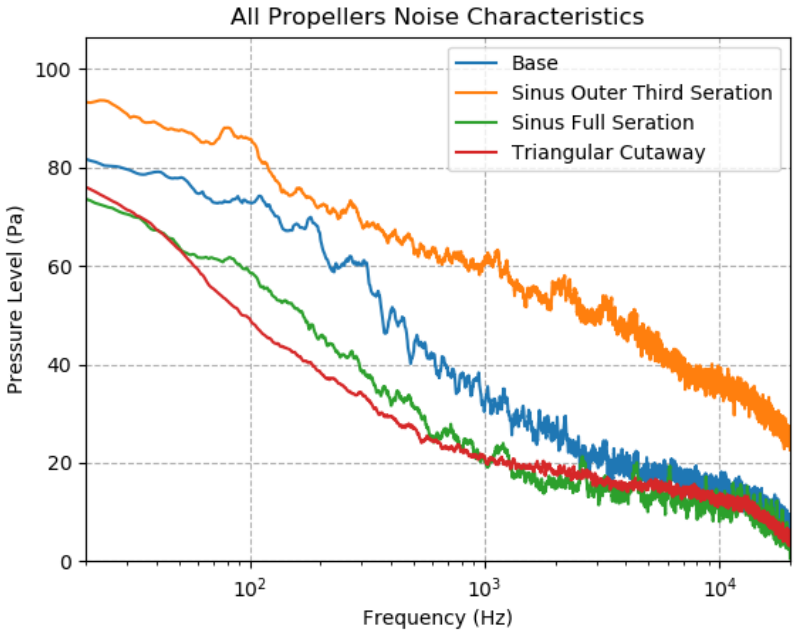

Figure 39: Pressure Spectrum of All 4 Propellers. Smoothed with a 30 Period Moving Average.

4.4 Case 2

For the second case the propeller with the triangular cutaway was dropped. It seemed more interesting to keep the propellers that were in the extremes of performance, and the principal design difference between the triangular modification and the partial sinusoidal modification was small.

4.5 Propeller Performance

The lift force for the three propellers is shown in Figure 40. Again, the lift force is proportional to the surface area of the propeller and the propeller wings that had the most surface removed showed the lowest lift force. The average lift force for this non rotational case is a bit lower than for the previous rotating case. It can be explained by the fact that the inlet velocity used – 19.0 m/s – is the velocity at half of the propeller radius for the rotating case. Combined with a propeller twist that is still present in the second it is to be expected that there is a small difference present. The difference is sufficiently small to give confidence in the case setup and to proceed to analysing noise emissions for the propellers.

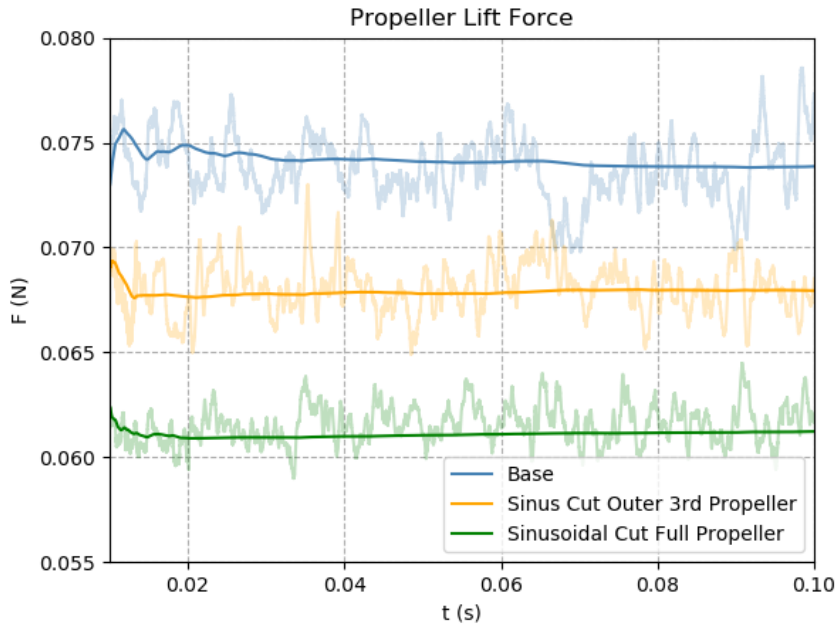

Figure 40: Lift Forces for the Propellers

4.6 Vortex Visualisation

A study of the vortexes for the second case reveals several interesting things. With the air flow over the propeller wing being fully developed, it is not as easy to see the contributions to the wake field made by the trailing edge of the wing. The vortexes from the trailing edge are obfuscated by the wakes from the turbulent fields that are present higher up at the wing. The area where the flow goes from laminar to turbulent is clearly seen, and matches the standard depiction of the flow over an airfoil that can be seen in various literature. For the purposes of this project, the origin of turbulent vortexes higher up than the trailing edge raises the important question whether this is an area that should have been targeted with the propeller modifications. Another interesting thing seen in the figures is how apparent the wing tip vortex is. This area could also have been targeted. Figure 41 shows the Q-criterion for the base propeller wing with an input value of 750 000 in Paraview.

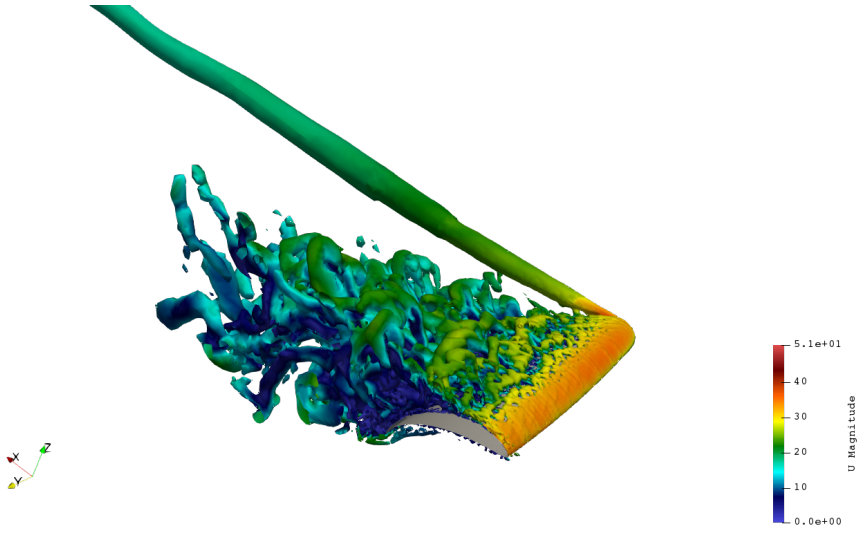

Figure 41: Q-vortices for the Base Propeller. Isosurfaces Computed at 750 000 in Paraview

Figure 42 shows the Sinus 3rd propeller. The difference between this and the base propeller is not very noticeable. The wing tip vortex is smaller which is probably due to the modification at the outer radius of the wing.

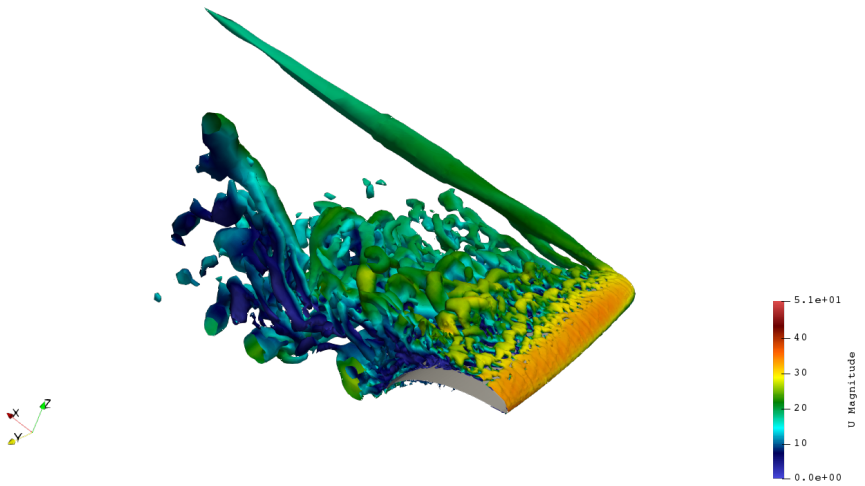

Figure 42: Q-vortices for the Sinus 3rd Propeller. Isosurfaces Computed at 750 000 in Paraview

Figure 43 shows the propeller with the full sinusoidal serration. It too has a smaller wing tip vortex than the base propeller, and although not very obvious, there seems to be less vortexes behind it compared to the other two propeller wings. It should be mentioned that comparing the number of vortices behind the propellers like this can be difficult, especially with instantaneous vortices like in these figures.

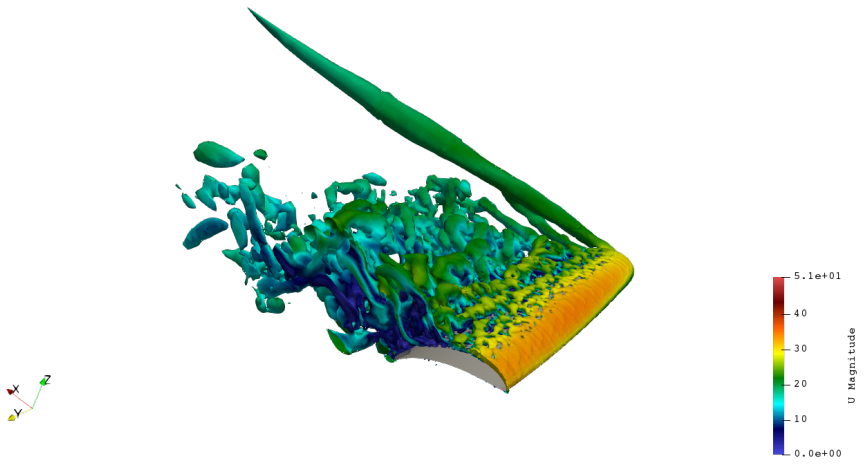

Figure 43: Q-vortices for the Full Sinus Propeller. Isosurfaces Computed at 750 000 in Paraview

4.7 Spectral Analysis

The spectral analysis of the second case was conducted using the observers that calculated the acoustic pressure using Curle's acoustic analogy. The noise characteristics of propellers in the second case differs from the results in the first case due to one significant difference which is the lack of tonal noise at the blade pass frequency and its harmonics. This feedback mechanism between the vortexes generated by the trailing edge and the interference with the leading edge is now gone, but a study of the trailing edge in the non rotational case is still of use because it shows what vortexes would have been generated. Starting at Observer 1 (see Figure 44), located at the wing tip, the modified propellers outperforms the base propeller across the entire frequency spectrum. There are no clear tones present but instead a broadband noise, for all propellers. One interesting thing that can be seen is that the Sinus Full Propeller outperforms the other propellers at the lower frequencies, but then has a higher frequency response around 10^4 Hz. This is most likely due to the serrations breaking down the larger vortices that generate a lower frequency sound, into smaller vortices that generate a higher frequency sound. Although there is an increase in sound pressure level at the higher frequency, that level is very low compared to the one at the lower frequencies. The higher frequencies are also damped faster in the air.

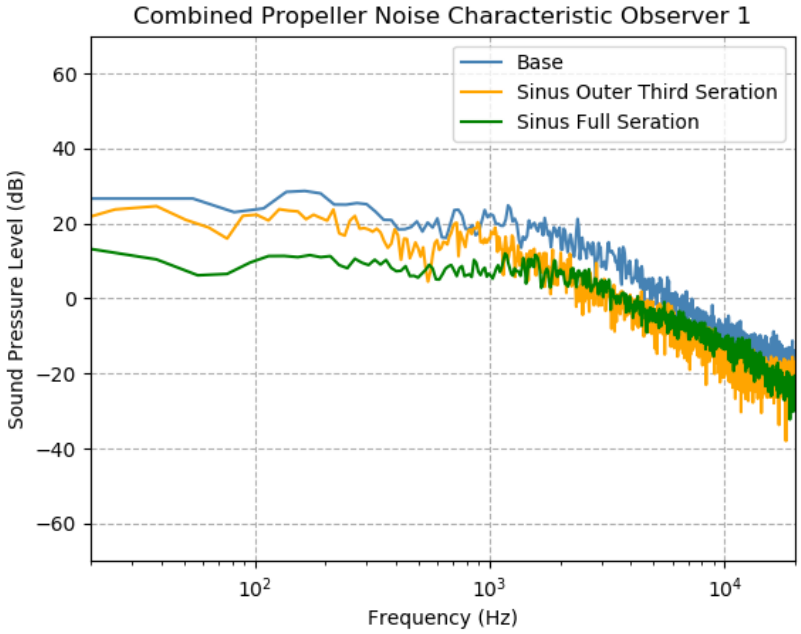

Figure 44: Spectrum of Sound Pressure Level at Observer 1

Going to observer 8 (see Figure 45), located at furthest point "after" the wing, the base propeller is once again outperformed by both modified propellers. Here there is a broader peak around the 1000 Hz area for all propellers. The Sinus Full Propeller shows an increase in the higher frequencies in this probe too.

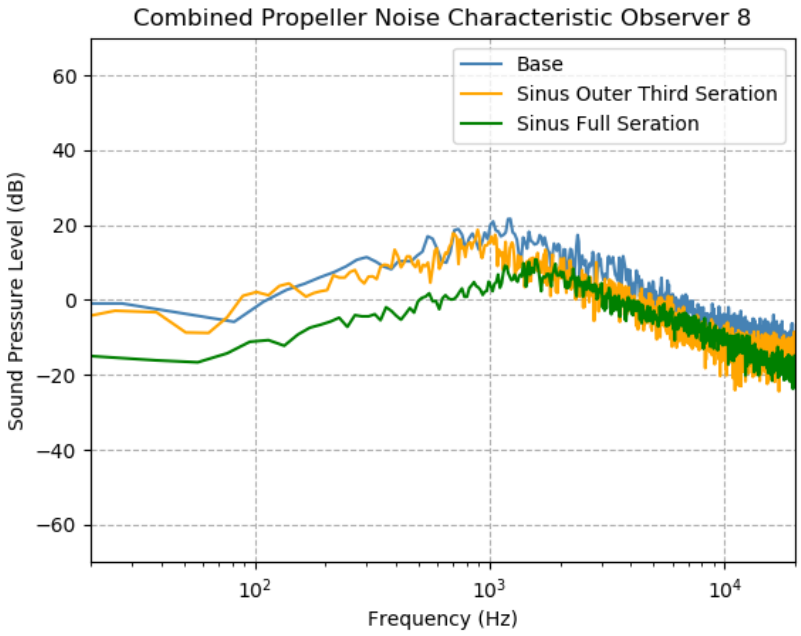

Figure 45: Spectrum of Sound Pressure Level at Observer 8

At observer 14 (seen in Figure 46), located at the highest point above the wing, there are no clear tones present, only broadband noise. Like at the other observers, the sound pressure level for the base propeller is the highest.

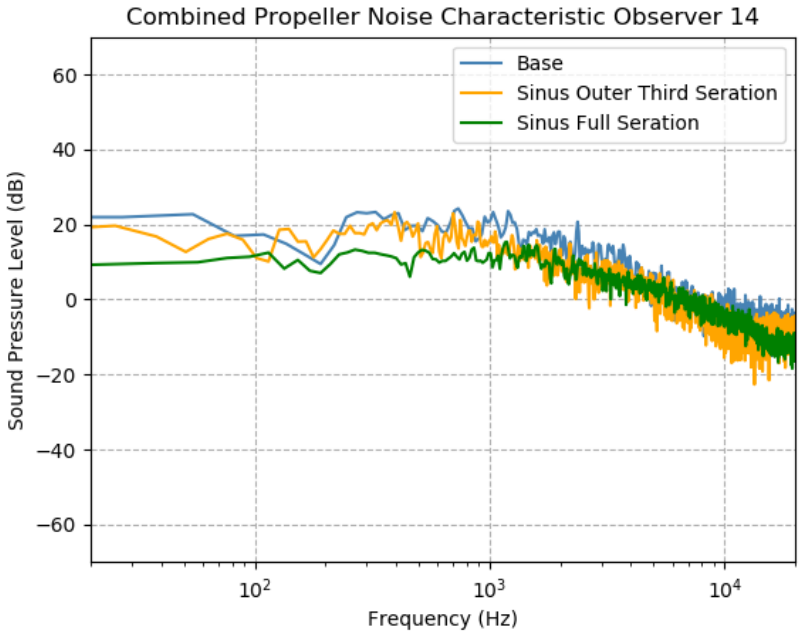

Figure 46: Spectrum of Sound Pressure Level at Observer 14

Observer 20 is located to the far left of the wing and at this observer the sound pressure level is very low. Once again, the base propeller seems to be the most noisy. The noise is made up of broadband noise. Observer 20 can be seen in Figure 47.

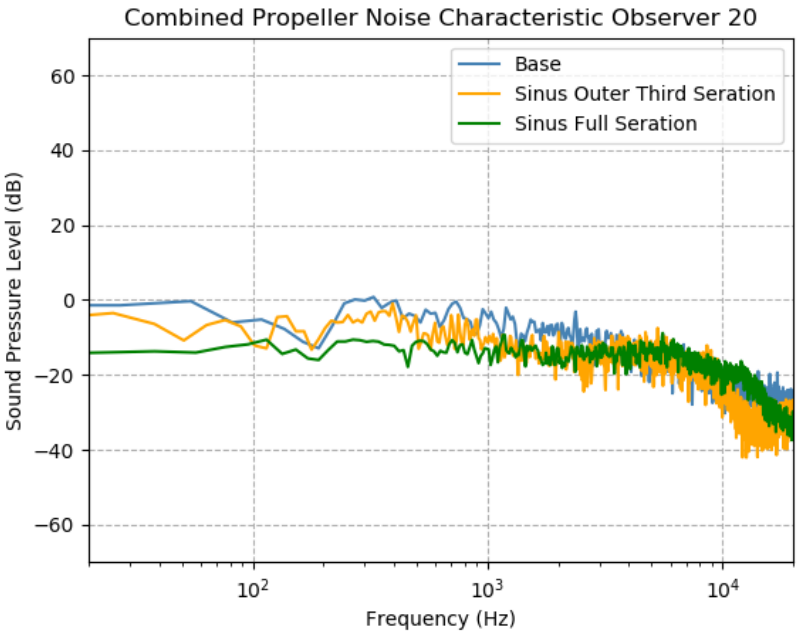

Figure 47: Spectrum of Sound Pressure Level at Observer 20

5 Conclusion

The purpose of this degree project has been to develop a low noise drone propeller using computational fluid dynamics simulations. A drone propeller from the manufacturer APC Propellers has been manufactured digitally and then been modified at the trailing edge since it has been observed in nature that such a feature on a wing reduced in flight noise. The different propellers manufactured have been analysed with different techniques and in different cases. One CFD case has been constructed using a single rotating domain and one using a non rotating rectangular domain. The reason for using two different setups is that both have had their limitations. Data has been collected from the simulations to study the noise both as generated from pressure points and from observers using Curle's acoustic analogy.

The results from the simulations shows that a modification to the trailing edge of a propeller can help reduce the noise that is generated. Both the tonal noise caused by the vortex feedback mechanism between leading and trailing edge as well as the overall sound level in the broadband component of the noise is reduced. However, a modification where material is removed as opposed to added, results in a reduction of propeller lift force. The place of the modification seems to play a big role in the overall sound characteristic of the propeller. A serration near the outer radius of the propeller does not seem to make as much of difference as one placed more at the center of the radius or closer to the hub. Out of the four propellers that were tested the one that had the best performance was the one with a sinusoidal cutaway along the entire trailing edge. The two propellers with modifications at their outer radii did show an overall better performance than the base propeller albeit not as much as expected. The modifications on these propellers did not eliminate the wing tip vortexes, which is not possible. The modifications did however seem to introduce fluctuations that did facilitate a quicker breakdown of the wing tip vortex, as seen in the vortex visualisation.

The analysis of the propeller and the qualitative analysis using the Q-criterion indicates that total noise that is generated from a drone propeller is a product of multiple factors – or locations on the propeller. This project only tries altering the structure in one location. When doing any sort of computer based design work, there is question whether the results are credible or not. During this project multiple strategies have been employed to ensure the validity of the results. First of the concept of altering the structure of a propeller in order to improve its noise characteristic was supported in previous scientific journals. A mesh sensitivity study was also made to see that the results from the simulations were reasonably accurate. The way the CFD simulations were setup should be emphasised when discussing whether the results are reasonable or not. The simulation design choices were choosed to best suit the application but still be reasonable in terms of computational expense. Despite this, some of the results showed inconsistencies. In the first case the Fourier Analysis showed that the sound characteristic of the propeller with a partial sinusoidal serration was much worse than the other propellers, including the base propeller. In the second case the same propeller performed better than the base propeller. This is likely due to a problem in the data collection or processing. It is possible that the probe locations for the first case was in a problematic area for that propeller and the results would have been different if probe data was available for other probes. However, sourcing that would have required the simulations to be run all over again and was just not possible – due to the time required to run them, despite using Aurora at LUNARC. The large amount of computing power that is required to run simulations with a turbulence model like LES also prevented the simulations to cover more than parts of a second.

In order to find out if the simulations have been correct one would have to create physical prototypes and recreate the experiments in the real world. Unfortunately that was not within the scope of this project but it is one of many things that can be done to further develop the designs, in the future.

5.1 Future Research and Improvements

This report documents the first iteration of a design and development process. The first iteration has largely consisted of constructing a framework, learning software and creating tools for development. The second iteration could probably be done one or even two orders of magnitude faster. If one were to make this second iteration there are some obvious and some not so obvious things to do.

In hindsight it seems obvious that creating a serration that adds surface area to the propeller is preferred to a serration that removes surface area. It is likely that such a serration would not cause the drop in lift force that was observed, and increase it instead.

The placement of the modifaction to the trailing edge could further be studied. The designs during the first iteration were in some ways arbitrary. It was thought that modifying the outer radius would provide the most benefit, but the studies showed otherwise. In the future a proper parameter study would need to be conducted, and possibilities for the choice of parameters are vast. One can both have parameters for the pattern (recall how it was mathematically driven) and for the placement.

Such a study could also be made in other areas of the propeller, such as the propeller wing tip and at the upper surface of the propeller wing. Some ideas to try are patterns like grooves or dimples on the surface. For the tip vortices there are various ways to construct winglets. In recent years, advances in manufacturing methods has made more exotic propeller shapes viable, such as the toroidal propeller. Such shapes would be interesting to evaluate.

The biggest improvement one can make to the testing would be to physically manufacture and test the propellers. This would leave no doubt whether the design changes works or not. Testing them with a real drone would also automatically introduce many good tests, suchs as propeller performance at different rpms, how the propellers work when there are several of them such as on a quadcopter, and what influence the body of the drone has on the noise. There are almost endless possibilites and this project has shown the use of computational fluid dynamics is a great tool in developing a low noise drone propeller.

References

[1] B. Schäffer, R. Pieren, K. Heutschi, J. M. Wunderli, and S. Becker, "Drone noise emission characteristics and noise effects on humans—a systematic review," *International Journal of Environmental Research and Public Health*, vol. 18, 11 Jun. 2021, ISSN: 16604601. DOI: 10.3390/ijerph18115940.

[2] A. News. "Drones banned from national parks in south australia to protect animals." (2016), [Online]. Available: https://www.abc.net.au/news/2016-09-03/drones-banned-from-sa-national-parks/7811416 (visited on 06/05/2023).

[3] G. V. Research. "Commercial drone market size, share trends analysis report by product, by application, by end-use, by region, and segment forecasts, 2021-2028." (2021), [Online]. Available: https://www.grandviewresearch.com/industry-analysis/global-commercial-drones-market (visited on 06/05/2023).

[4] P. Sagar, P. Teotia, A. D. Sahlot, and H. Thakur, "An analysis of silent flight of owl," *Materials Today: Proceedings*, vol. 4, no. 8, pp. 8571–8575, 2017, International Conference on Advancements in Aeromechanical Materials for Manufacturing (ICAAMM-2016): Organized by MLR Institute of Technology, Hyderabad, Telangana, India, ISSN: 2214-7853. DOI: https://doi.org/10.1016/j.matpr.2017.07.204. [Online]. Available: https://www.sciencedirect.com/science/article/pii/S2214785317315018 (visited on 06/05/2023).

[5] F. E. Hitchens, *Propeller Aerodynamics*. Andrews UK Limited, 2015, ch. 1, pp. 9–12.

[6] NASA. "Bernoulli and newton." (2021), [Online]. Available: https://www.grc.nasa.gov/www/k-12/VirtualAero/BottleRocket/airplane/bernnew.html (visited on 06/05/2023).

[7] NASA, *Lift from flow turning*, 2021. [Online]. Available: https://www.grc.nasa.gov/www/k-12/airplane/right2.html (visited on 06/05/2023).

[8] D. A. Bies and C. H. Hansen, *Engineering Noise Control: Theory and Practice, Fourth Edition*. CRC Press, 2009, ch. 2.

[9] F. E. Hitchens, *Propeller Aerodynamics*. Andrews UK Limited, 2015, ch. 5, p. 123.

[10] C. Doolan, Y. Yauwenas, and D. Moreau, "Drone propeller noise under static and steady inflow conditions," in *Flinovia—Flow Induced Noise and Vibration Issues and Aspects-III*, E. Ciappi, S. De Rosa, F. Franco, *et al.*, Eds., Cham: Springer International Publishing, 2021, pp. 45–60, ISBN: 978-3-030-64807-7.

[11] P. Candeloro, D. Ragni, and T. Pagliaroli, *Small-scale rotor aeroacoustics for drone propulsion: A review of noise sources and control strategies*, Aug. 2022. DOI: 10.3390/fluids7080279.

[12] H. K. Versteeg and W Malalasekera, *An Introduction to Computational Fluid Dynamics*. Addison-Wesley Professional, 2007, ch. 2, pp. 9–11.

[13] F Moukalled, L Mangani, and M Darwish, *Fluid Mechanics and Its Applications The Finite Volume Method in Computational Fluid Dynamics*. Springer, ch. 4, p. 111. [Online]. Available: http://www.springer.com/series/5980.

[14] F. Moukalled, L. Mangani, and M. Darwish, "Solving the system of algebraic equations," in *The Finite Volume Method in Computational Fluid Dynamics: An Advanced Introduction with OpenFOAM® and Matlab*. Cham: Springer International Publishing, 2016, pp. 303–364, ISBN: 978-3-319-16874-6. DOI: 10.1007/978-3-319-16874-6_10. [Online]. Available: https://doi.org/10.1007/978-3-319-16874-6_10 (visited on 06/05/2023).

[15] T. Holzmann, *Mathematics, Numerics, Derivations and OpenFOAM(R)*. 2019. [Online]. Available: https://Holzmann-cfd.de (visited on 06/05/2023).

[16] F. Moukalled, L. Mangani, and M. Darwish, "Turbulence modeling," in *The Finite Volume Method in Computational Fluid Dynamics: An Advanced Introduction with OpenFOAM® and Matlab*. Cham: Springer International Publishing, 2016, pp. 693–744, ISBN: 978-3-319-16874-6. DOI: 10.1007/978-3-319-16874-6_17. [Online]. Available: https://doi.org/10.1007/978-3-319-16874-6_17.

[17] M. J. Lighthill, "On sound generated aerodynamically i. general theory," *Proceedings of the Royal Society of London. Series A. Mathematical and Physical Sciences*, vol. 211, 1107 1952, ISSN: 0080-4630. DOI: 10.1098/rspa.1952.0060.

[18] N. Curle, "The Influence of Solid Boundaries upon Aerodynamic Sound," *Proceedings of the Royal Society of London Series A*, vol. 231, no. 1187, Sep. 1955. DOI: 10.1098/rspa.1955.0191.

[19] H.-D. Yao, L. Davidson, L.-E. Eriksson, O. Grundestam, S.-H. Peng, and P. E. Eliasson, "Surface integral analogy approaches to computing noise generated by a 3d high-lift wing configuration," 2012, pp. 9–12.

[20] R. Noda, T. Nakata, T. Ikeda, *et al.*, "Development of bio-inspired low-noise propeller for a drone," *Journal of Robotics and Mechatronics*, vol. 30, pp. 337–343, 3 Jun. 2018, ISSN: 18838049. DOI: 10.20965/jrm.2018.p0337.

[21] D. Li, X. Liu, F. Hu, and L. Wang, "Effect of trailing-edge serrations on noise reduction in a coupled bionic aerofoil inspired by barn owls," *Bioinspiration and Biomimetics*, vol. 15, 1 2020, ISSN: 17483190. DOI: 10.1088/1748-3190/ab529e.

[22] F. Nozaki, *CFD for rotating machinery*. [Online]. Available: https://www.slideshare.net/fumiyanozaki96/cfd-for-rotating-machinery-using-openfoam (visited on 06/05/2023).